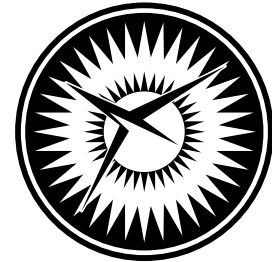


NASA/CR-2005-213915
NIA Report No. 2005-06



NATIONAL
INSTITUTE OF
AEROSPACE



Skin-Stiffener Debond Prediction Based on Computational Fracture Analysis

Ronald Krueger
National Institute of Aerospace, Hampton, Virginia

Pierre J. Minguet
The Boeing Company, Philadelphia, Pennsylvania

September 2005

The NASA STI Program Office . . . in Profile

Since its founding, NASA has been dedicated to the advancement of aeronautics and space science. The NASA Scientific and Technical Information (STI) Program Office plays a key part in helping NASA maintain this important role.

The NASA STI Program Office is operated by Langley Research Center, the lead center for NASA's scientific and technical information. The NASA STI Program Office provides access to the NASA STI Database, the largest collection of aeronautical and space science STI in the world. The Program Office is also NASA's institutional mechanism for disseminating the results of its research and development activities. These results are published by NASA in the NASA STI Report Series, which includes the following report types:

- **TECHNICAL PUBLICATION.** Reports of completed research or a major significant phase of research that present the results of NASA programs and include extensive data or theoretical analysis. Includes compilations of significant scientific and technical data and information deemed to be of continuing reference value. NASA counterpart of peer-reviewed formal professional papers, but having less stringent limitations on manuscript length and extent of graphic presentations.
- **TECHNICAL MEMORANDUM.** Scientific and technical findings that are preliminary or of specialized interest, e.g., quick release reports, working papers, and bibliographies that contain minimal annotation. Does not contain extensive analysis.
- **CONTRACTOR REPORT.** Scientific and technical findings by NASA-sponsored contractors and grantees.

- **CONFERENCE PUBLICATION.** Collected papers from scientific and technical conferences, symposia, seminars, or other meetings sponsored or co-sponsored by NASA.
- **SPECIAL PUBLICATION.** Scientific, technical, or historical information from NASA programs, projects, and missions, often concerned with subjects having substantial public interest.
- **TECHNICAL TRANSLATION.** English-language translations of foreign scientific and technical material pertinent to NASA's mission.

Specialized services that complement the STI Program Office's diverse offerings include creating custom thesauri, building customized databases, organizing and publishing research results ... even providing videos.

For more information about the NASA STI Program Office, see the following:

- Access the NASA STI Program Home Page at <http://www.sti.nasa.gov>
- E-mail your question via the Internet to help@sti.nasa.gov
- Fax your question to the NASA STI Help Desk at (301) 621-0134
- Phone the NASA STI Help Desk at (301) 621-0390
- Write to:
NASA STI Help Desk
NASA Center for AeroSpace Information
7121 Standard Drive
Hanover, MD 21076-1320

NASA/CR-2005-213915
NIA Report No. 2005-06



Skin-Stiffener Debond Prediction Based on Computational Fracture Analysis

Ronald Krueger
National Institute of Aerospace, Hampton, Virginia

Pierre J. Minguet
The Boeing Company, Philadelphia, Pennsylvania

National Aeronautics and
Space Administration

Langley Research Center
Hampton, Virginia 23681-2199

Prepared for Langley Research Center
under Contract NAS1-02117

September 2005

Available from:

NASA Center for AeroSpace Information (CASI)
7121 Standard Drive
Hanover, MD 21076-1320
(301) 621-0390

National Technical Information Service (NTIS)
5285 Port Royal Road
Springfield, VA 22161-2171
(703) 605-6000

SKIN-STIFFENER DEBOND PREDICTION BASED ON COMPUTATIONAL FRACTURE ANALYSIS

Ronald Krueger¹ and Pierre J. Minguet²

ABSTRACT

Interlaminar fracture mechanics has proven useful for characterizing the onset of delaminations in composites and has been used with limited success primarily to investigate onset in fracture toughness specimens and laboratory size coupon type specimens. Future acceptance of the methodology by industry and certification authorities however, requires the successful demonstration of the methodology on structural level. For this purpose a panel was selected that is reinforced with stringers. Shear loading causes the panel to buckle and the resulting out-of-plane deformations initiate skin/stringer separation at the location of an embedded defect. For finite element analysis, the panel and surrounding load fixture were modeled with shell elements. A small section of the stringer foot and the panel in the vicinity of the embedded defect were modeled with a local 3D solid model. Across the width of the stringer foot the mixed-mode strain energy release rates were calculated using the virtual crack closure technique. A failure index was calculated by correlating the results with the mixed-mode failure criterion of the graphite/epoxy material. For small applied loads the failure index is well below one across the entire width. With increasing load the failure index approaches one first near the edge of the stringer foot from which delamination is expected to grow. With increasing delamination lengths the buckling pattern of the panel changes and the failure index increases which suggests that rapid delamination growth from the initial defect is to be expected.

1. BACKGROUND

Many composite components in aerospace structures are made of flat or curved panels with co-cured or adhesively bonded frames and stiffeners. Recent studies focused on the investigation of the debonding mechanism and included testing of skin/stiffener panels and failure analysis using shell models [1-4]. Over the last decade a consistent step-wise approach has been developed which uses experiments to detect the failure mechanism, computational stress analysis to determine the location of first matrix cracking and computational fracture mechanics to investigate the potential for delamination growth. Testing of skin gage stiffened panels designed for pressurized aircraft fuselage has shown that bond failure at the tip of the frame flange is an important and very likely failure mode [5]. Comparatively simple specimens consisting of a stringer flange bonded onto a skin have been developed to study skin/stiffener debonding [6-8]. The failure that initiates at the tip of the flange in these specimens is nearly identical to the failure observed in the full-scale panels and the frame pull-off specimens [7, 9, 10]. A methodology based on fracture mechanics [11] has proven useful for characterizing the onset and growth of delaminations in composites and has been used with limited success primarily to investigate delamination onset and debonding in simple characterization specimens

¹ Senior Staff Scientist, National Institute of Aerospace (NIA), 100 Exploration Way, Hampton, VA 23666.

² The Boeing Company, Philadelphia, Pennsylvania

as shown in Figure 1a and laboratory size coupon type specimens such as the skin/stringer debond specimen shown in Figure 1b,c [9, 10]. Future acceptance of the methodology by industry and certification authorities however, requires the successful demonstration of the methodology on structural level.

The objective of this research was to demonstrate the application of the fracture mechanics based methodology on structural level for which a panel made of IM7/8552 carbon/epoxy tape was selected. The 1,016-mm by 1,016-mm wide panel shown in Figure 1d is reinforced with three stringers made of IM7/8552 carbon/epoxy plain weave fabric. An artificial defect was placed at the termination of the center stiffener. The stiffened panel is subjected to pure shear loading which causes the panel to buckle. The resulting out-of-plane deformation causes skin/stringer separation at the location of the initial defect. For finite element analysis the entire panel was modeled with shell elements. Locally the vicinity of the debonded section is modeled with solid elements. During a series of nonlinear finite element analyses, strain energy release rates and mixed mode ratios were computed using the virtual crack closure technique (VCCT). The analyses were performed for four delamination lengths and results were correlated to the mixed-mode fracture toughness of the composite material.

2. METHODOLOGY

2.1. Interlaminar Fracture Mechanics

Interlaminar fracture mechanics has proven useful for characterizing the onset and growth of delaminations [11, 12]. The total strain energy release rate, G_T , the mode I component due to interlaminar tension, G_I , the mode II component due to interlaminar sliding shear, G_{II} , and the mode III component, G_{III} , due to interlaminar scissoring shear, as shown in Figure 2, need to be calculated. In order to predict delamination onset or growth for two-dimensional problems, these calculated G components are compared to interlaminar fracture toughness properties measured over a range of mode mixities from pure mode I loading to pure mode II loading [13-15].

A quasi static mixed-mode fracture criterion is determined by plotting the interlaminar fracture toughness, G_c , versus the mixed-mode ratio, G_{II}/G_T , determined from data generated using pure Mode I ($G_{II}/G_T=0$) Double Cantilever Beam (DCB) pure Mode II ($G_{II}/G_T=1$) four point End Notched Flexure (4ENF), and Mixed Mode Bending (MMB) tests of varying ratios as shown in Figure 3 for IM7/8852 carbon epoxy material. A curve fit to the experimental data is performed using a failure criterion suggested in [16] to determine a mathematical relationship between G_c and G_{II}/G_T .

$$G_c = G_{Ic} + (G_{IIc} - G_{Ic}) \cdot \left(\frac{G_{II}}{G_T} \right)^\eta$$

where G_{Ic} and G_{IIc} are the fracture toughness data for mode I and II and η is a factor determined by the curve fit. Failure is expected when, for a given mixed mode ratio G_{II}/G_T , the calculated total energy release rate, G_T , exceeds the interlaminar fracture toughness, G_c . Although several test methods have been suggested for the measurement of the mode III

interlaminar fracture toughness property [17-19], an interaction criterion incorporating the scissoring shear, however, has not yet been established. The edge-cracked torsion test (ECT) is being investigated for standardization of this fracture mode [20, 21].

2.2. Analysis Tools

2.2.1. Virtual Crack Closure Technique

For delaminations in laminated composite materials where the failure criterion is highly dependent on the mixed-mode ratio and propagation occurs in the laminate plane, the virtual crack closure technique [22, 23] has been most widely used for computing energy release rates because fracture mode separation is determined explicitly. The Virtual Crack Closure Technique requires force and displacement input, which is obtained from continuum (2-D) and solid (3-D) finite element analyses of the cracked (2-D) or delaminated (3-D) component.

The mode I, and mode II components of the strain energy release rate, G_I and G_{II} are calculated for four-noded elements as shown in Figure 4a

$$G_I = -\frac{1}{2\Delta a} \cdot Z_i \cdot (w_\ell - w_{\ell^*})$$

$$G_{II} = -\frac{1}{2\Delta a} \cdot X_i \cdot (u_\ell - u_{\ell^*})$$

where Δa is the length of the elements at the crack front and X_i and Z_i are the forces at the crack tip (nodal point i). The relative displacements behind the crack tip are calculated from the nodal displacements at the upper crack face u_ℓ and w_ℓ (nodal point ℓ) and the nodal displacements u_{ℓ^*} and w_{ℓ^*} at the lower crack face (nodal point ℓ^*) respectively. The crack surface ΔA created is calculated as $\Delta A = \Delta a \cdot 1$, where it is assumed that the two-dimensional model is of unit thickness "1".

For geometric nonlinear analysis where large deformations may occur, both forces and displacements obtained in the global coordinate system need to be transformed into a local coordinate system (x' , z') which originates at the crack tip as shown in Figure 4b. The local crack tip system defines the tangential (x' , or mode II) and normal (z' , or mode I) coordinate directions at the crack tip in the deformed configuration. The equations to calculate the mixed-mode energy release rate components remain the same as before, with forces and displacements now expressed in the local system. For the two-dimensional eight-noded quadrilateral element with quadratic shape functions this yields

$$G_I = -\frac{1}{2\Delta a} \cdot Z'_i \cdot (w'_\ell - w'_{\ell^*})$$

$$G_{II} = -\frac{1}{2\Delta a} \cdot X'_i \cdot (u'_\ell - u'_{\ell^*})$$

where X'_i, Z'_i are the forces at the crack tip at nodal point i and u'_{ℓ} and w_{ℓ} (u'_{ℓ^*}, w'_{ℓ^*}) are the displacements at the corresponding nodal points ℓ and ℓ^* behind the crack tip. The total energy release rate G_T is calculated from the individual mode components as

$$G_T = G_I + G_{II} + G_{III}$$

where $G_{III}=0$ for the two-dimensional case discussed.

In a finite element model made of three-dimensional solid elements the delamination of length a is represented as a two-dimensional discontinuity by two surfaces. The additional dimension allows to calculate the distribution of the energy release rates along the delamination front and makes it possible to obtain G_{III} , which is identical to zero for two-dimensional models. For convenience, only a section of the delaminated area which is modeled with eight-noded three-dimensional solid elements is illustrated in Figure 5. The mode I, mode II, and mode III components of the strain energy release rate, G_I , G_{II} , and G_{III} are calculated as

$$G_I = -\frac{1}{2\Delta A} \cdot Z_{Li} \cdot (w_{L\ell} - w_{L\ell^*})$$

$$G_{II} = -\frac{1}{2\Delta A} \cdot X_{Li} \cdot (u_{L\ell} - u_{L\ell^*})$$

$$G_{III} = -\frac{1}{2\Delta A} \cdot Y_{Li} \cdot (v_{L\ell} - v_{L\ell^*})$$

with $\Delta A = \Delta a \cdot b$ as shown in Figure 5. Here ΔA is the area virtually closed, Δa is the length of the elements at the delamination front, and b is the width of the elements. For better identification in this and the following figures, columns are identified by capital letters and rows by small letters as illustrated in the top view of the upper surface shown in Figure 4b. Hence, X_{Li}, Y_{Li} and Z_{Li} denote the forces at the delamination front in column L , row i . The corresponding displacements behind the delamination at the top face node row ℓ are denoted $u_{K\ell}, v_{K\ell}$ and $w_{K\ell}$ and at the lower face node row ℓ are denoted $u_{K\ell}, v_{K\ell}$ and $w_{K\ell}$ as shown in Figure 5. All forces and displacements are obtained from the finite element analysis with respect to the global system. A local crack tip coordinate system (x', y', z'), that defines the normal and tangential coordinate directions at the delamination front in the deformed configuration, has been added to the illustration. Its use with respect to geometrically nonlinear analyses was discussed above.

2.2.2. A Global/Local Shell 3D Modeling Technique

Built-up structures are traditionally modeled and analyzed using plate or shell finite elements as shown in Figure 1d to keep the modeling and computational effort affordable. Computed mixed mode strain energy release rate components, however, depend on many variables such as element order and shear deformation assumptions, kinematic constraints in the neighborhood of the delamination front, and continuity of material properties and section stiffness in the vicinity of the debond when delaminations or debonds are modeled with plate or shell finite elements [24-26]. These problems may be avoided by using three-dimensional models as shown in Figures 1a and b. Since many layers of brick elements through the thickness

are often necessary to model the individual plies, however, the number of degrees of freedom in a finite element model may become prohibitively large.

For detailed modeling and analysis of the delaminations, the shell/3D modeling technique will reduce the modeling time since existing plate or shell models may be modified to shell/3D models. This is a considerable advantage compared to the creation of an entirely new three-dimensional finite element model. The technique will also reduce computational time because only a relatively small section of interest needs to be modeled with solid elements reducing the number of unknowns. The technique combines the accuracy of the full three-dimensional solution with the computational efficiency of a plate or shell finite element model and has been demonstrated for various applications such as fracture toughness characterization specimens and on coupon level for the skin/stringer separation specimen as shown in Figures 1c [13, 27-29].

3. FINITE ELEMENT MODELING

For the demonstration of the methodology on structural level the stringer stiffened panel as shown in Figure 6 was selected. The 1,016 mm by 1,016 mm wide panel made of IM7/8552 carbon/epoxy tape is reinforced with three stringers made of IM7/8552 carbon/epoxy plain weave fabric. The stiffened panel is bolted to a steel picture frame as shown in Figure 6a. Shear is induced in the panel through the frame reaction to the externally applied tensile load. During manufacturing an artificial defect had been placed at the termination of the center stiffener as shown in the sketch of Figure 6b. The shear loading leads the panel to buckle as visible in the photograph of Figure 6a. The resulting out-of-plane deformation causes skin/stringer separation at the location of the initial defect.

3.1. Global Shell Model of Stringer Stiffened Panel

The global model includes the steel load frame and attachments, the panel made of graphite/epoxy prepreg tape and the stringers made of graphite/epoxy fabric as shown in Figure 7. The outer steel load frame and the attachment bolts were modeled with beam elements available in the finite element software ABAQUS[®] as shown in Figure 7a. The inner steel load frame which overlaps the panel edge was modeled with standard shell S4 elements. Shell elements were also used to model the panel bay, the reinforced panel bay and the reinforced panel perimeter as shown in Figure 7a. The stiffener components, such as foot, web and hat as shown in Figure 7b, were also modeled with S4 shell elements.

A detail of the global finite element model in the vicinity of the stringer termination is shown in Figure 8a. The stacking sequence for the different skin/stringer components are shown in Figure 8b. In the detail it is clearly visible that the panel skin and the stiffener foot are modeled as separate offset entities. The S4 shell elements are located at the panel skin and stiffener foot respective mid-planes. The shell elements are connected by beam elements designed to enforce plate theory constraints [30]. In the sections containing the artificial defects the beam elements were replaced by gap elements. The gap elements allow the modeling of the skin/stringer separation but also prevent element interpenetration in case the surfaces get into contact.

In preparation for the global/local modeling approach shell elements representing the foot of the stiffener and the panel were removed from the original shell model around the center

stringer termination as shown in Figure 9. The shell elements used to model the stiffener web and hat were kept in place. At the boundaries shell edges in ABAQUS[®] were defined as shown which were used to connect the shell model with the local 3D insert model using the shell to solid coupling option in ABAQUS[®] which allows the connection between non-conforming shell and solid models.

3.2. Local 3D Insert Model for Solid Modeling of the Stringer Foot and Panel Skin

The local 3D insert model was generated using C3D8I solid brick elements and consisted of an intact section and a delaminated section with a fine mesh around the delamination front as shown in Figure 10a. Surfaces were defined in ABAQUS on the outer faces of the insert model to provide a connection with the global shell model using the shell to solid coupling option in ABAQUS[®]. The initial defect is located at the bondline between stringer foot and the panel. This defect was treated as a delamination and modeled as a discrete discontinuity using two unconnected nodes with identical coordinates one on each side of the delamination. A refined mesh was used along the stringer boundary in order to capture edge effects as shown in Figure 10b. Using the finite sliding option available in ABAQUS[®] contact was modeled between the delaminated surfaces to avoid interpenetration during analysis. Four elements over the thickness were used to model the foot of the stiffener made of carbon/epoxy fabric as shown in Figure 10b. The -45° skin ply made carbon/epoxy tape which is adjacent to the plane of delamination was modeled with one element. The remaining 10 plies of carbon/epoxy tape were modeled with three elements over the thickness as shown in Figure 10b.

3.3. Combined Global/Local Shell/3D Model of Stringer Stiffened Panel

For modeling the experiment, which was performed under constant displacement control, as closely as possible uniform displacements u, v were applied at one corner node to introduce shear as shown in Figure 11a. The inplane displacements u, v were suppressed at the diagonally opposite corner and the out of plane displacements w were suppressed along all four edges across the entire width of the inner and outer steel load frame. The local 3D insert model containing a straight delamination front was inserted into the global shell model as shown in the detail of Figure 11b. The local 3D insert model consisted of an intact section and a delaminated section of length a with a fine mesh around the delamination front as discussed above. The global shell model was connected to the local 3D insert model using the shell to solid coupling option in ABAQUS[®] which allows the connection between non-conforming shell and solid models. For the entire analyses the non-linear solution option was used in ABAQUS[®].

A total of eight delamination lengths were modeled ($a=81.9$ mm, 88.9 mm, 94.9 mm, 101.6 mm, 127.0 mm, 203.2 mm, 279.4 mm and 355.6 mm). The initial length corresponds to the length of insert used to create an initial defect at the termination of the center stringer as shown in Figure 6. Additional lengths were chosen to study the change in energy release rate distribution across the width (b) of the stringer with increasing delamination length (a). A short local 3D insert as shown in Figures 12a - where $c=116.7$ mm of the stringer foot and panel skin were modeled with CD8I solid brick elements - was used to model a total of four delamination lengths ($a=81.9$ mm, 88.9 mm, 94.6 mm, and 101.6 mm). A longer local 3D insert - where $c=431.2$ mm of the stringer foot and panel skin were modeled with CD8I solid brick elements -

was used to model the delamination lengths from $a=127.0$ mm to $a=355.6$ mm as shown in Figure 12b.

4. ANALYSIS RESULTS

4.1. Deformed Panel

The deformed finite element models of the stiffened panel are shown in Figures 13 and 14. The color contour plots illustrate the out-of-plane deformation w designated u_3 in ABAQUS. The color limits were set for the last analysis increment after the entire external displacement $u=v=6.35$ mm had been applied during the analysis of the panel with a simulated delamination length $a=81.9$ mm. The limits were kept unchanged for all plots ranging from dark blue for the trough to bright red for the peak. For the panel with a short local insert and a simulated delamination length $a=81.9$ mm three peaks and one trough can be observed in the panel bays adjacent to the center stiffener as shown in Figure 13a. For longer delaminations modeled the buckling pattern changed as shown in Figure 13b for a simulated delamination length $a=101.6$ mm. The longer delamination caused a change in the stiffness which resulted in an altered buckling pattern. In one panel bay one peak disappeared and the trough became more pronounced. Out-of-plane displacements which exceeded the previously set color limits are shown in black for the trough and white for the peak. The buckling pattern remained unchanged for the panel with a long local insert and a simulated delamination length $a=127.0$ mm as shown in Figure 14a. Another change in the global buckling pattern was observed for a simulated delamination length $a=355.6$ mm as shown in Figure 14b. The analysis terminated prematurely due to convergence problems after only 83% of the external displacement had been applied. The new pattern only had one pronounced peak. Additionally another trough formed and the original trough extended to both bays adjacent to the center stringer.

The detail of the deformed local models are shown in Figures 15-18. For a delamination length $a=81.9$ mm details of the deformed local models are shown in Figure 15 for different analysis increments. Early in the analysis (increment 5) a mode I opening was observed only near one edge as shown in Figure 15a. With increasing applied external displacement the deformation changed locally and for increment 15 mode I disappeared completely and the delamination appeared closed over the entire delaminated length. A small scissoring shear (mode III) could be observed as shown in Figure 15b. Further increasing the external displacement resulted in a small mode I opening across the entire width of the stringer as observed for increment 20 as shown in Figure 15c. For the last step of the analysis (increment 41) after the entire external displacement $u=v=6.35$ mm had been applied mode I opening was observed across the entire width of the stringer over the entire delaminated length as shown in Figures 15d and e. The same opening is also observed for modeled delamination lengths $a=88.9$ mm and 94.9 mm as shown in Figures 16a and b. The detail of the deformed local model for a delamination length $a=101.6$ mm is shown in Figure 16c for the last analysis increment. The figure reveals that not the entire delaminated section opens under mode I. After initial opening, the section below the web termination closes and the delaminated surfaces contact. This closing is caused by a change in the local buckling pattern, due to stiffness changes caused by the longer delamination, as discussed above. It was observed that the local buckling pattern in the immediate surrounding of the delaminated stringer is dependent on the delamination length modeled, which made convergence difficult.

The detail of the deformed long local 3D insert model for a delamination length $a=127.0$ mm is show in Figure 17a also for the last analysis increment after the entire external displacement $u=v=6.35$ mm had been applied. Although opening of the entire delaminated section is observed, the deformed shape is similar to the deformation shown in Figure 16c for a delamination length $a=101.6$ mm. For both cases the closing at the web termination is caused by a change in the local buckling pattern. The detail of the deformed local model for a delamination length $a=203.2$ mm is show in Figure 17b after only 83% of the external displacement had been applied. The analysis terminated prematurely due to convergence problems. For the model representing a delamination length of $a=279.4$ mm an opening of the delaminated section is observed for the entire delamination length modeled as shown in Figure 18a. Partial closure of the delaminated surfaces which result in local contact is observed for the analysis of the $a=355.6$ mm delamination as shown in Figure 18b.

4.2. Calculation of Mixed-Mode Strain Energy Release Rates and Failure Indices

The virtual crack closure technique (VCCT) – discussed earlier - was used to calculate the mode contributions G_I , G_{II} and G_{III} the total energy release rate $G_T=G_I+G_{II}+G_{III}$, as well as the mixed mode ratios G_S/G_T along the delamination front across the width b of the stringer for all delamination lengths modeled. Here G_S denotes the sum of the in-plane shearing components $G_{II}+G_{III}$. For two-dimensional analyses, where $G_{III}=0$, this definition is equal to the commonly used definition of the mixed mode ratio, G_{II}/G_T . For three-dimensional analysis, which also yields results for the scissoring mode G_{III} , the modified definition of G_S is introduced since a mixed-mode failure criterion, which accounts for all three modes is currently not available.

For each nodal point along the delamination front the critical energy release rate G_c was calculated from the mixed mode failure criterion for IM7/8552 graphite/epoxy (Figure 3)

$$G_c = 207.7 + 1126.8 \cdot \left(\frac{G_S}{G_T} \right)^{4.46} .$$

for the computed mixed-mode ratio G_S/G_T at each point. Subsequently the failure index G_T/G_c was determined with the assumption that delamination propagation occurs for

$$\frac{G_T}{G_c} \geq 1.$$

For all delamination lengths modeled, the computed failure indices were calculated for every fifth increment plus the final increment of the analysis and plotted versus the dimensionless coordinate s across the width of the stringer b

$$s(y) = \frac{y - y_0}{b}; \quad 0.0 \leq s \leq 1.0 .$$

At the left edge of the stringer the nodal point coordinates are equal to $y=y_0$ which yields $s=0.0$ and the right edge nodal point coordinates are equal to $y=y_b$ which results in $s=1.0$ as depicted in Figure 11.

Shown as example are the mode contributions G_I , G_{II} and G_{III} and the total energy release rate $G_T=G_I+G_{II}+G_{III}$ for increment 5 (Figure 19) and the last increment 41 (Figure 20) for a modeled delamination length of $a=81.9$ mm. The results indicated that the distribution across the width changes during the analysis. The analysis also revealed a significant mode III contribution for the problem investigated. The computed total energy release rates G_T for all increments are plotted in Figure 21. The total energy release rates peaks at the edges ($s=0.0$ and $s=1.0$) with an additional peak around the center ($s\sim 0.5$) underneath the stringer web. Selected mixed mode ratio G_{II}/G_T distributions are shown in Figure 22 and appear to be dependent on the applied load. Early in the analysis (increment 5) mode I opening is observed near one edge and in the center on stringer. The other delamination at the other edge does not open and ratio $G_{II}/G_T=1$. For increment 20 mode I disappears completely which indicates that the delamination is closed almost along the entire front. For the last step of the analysis (increment 41) mode I opening is observed over almost the entire width of specimen except for one small region near one edge. The change in the distributions is caused by the change in local buckling pattern with increasing load.

For all delamination lengths modeled, the calculated failure indices are shown in Figures 23 to 30 for selected increments only. For delamination lengths up $a=94.9$ mm the failure index peaks at the edges ($s=0.0$ and $s=1.0$) with an additional peak around the center ($s\sim 0.5$) underneath the stringer web, as shown in Figures 23 to 25. Early in the analysis (small increment numbers), which corresponds to small applied displacements, the failure index G_T/G_c is well below one across the entire width. This result indicates that the delamination is not going to grow. With increasing load the failure index approaches one first near one edge where failure is expected to initiate. Generally, for the next load increment, the index is well above one across the entire width. For the longer delaminations ($a=101.6$ mm and $a=355.6$ mm) which are associated with a different global buckling pattern, the distribution across the width changes, the failure index peaks in the center underneath the stringer web and is reduced toward the edges as shown in Figures 26 and 30. As before, the failure index G_T/G_c remains well below one across the entire width for small increment numbers, which corresponds to small applied displacements. With increasing load, the failure index first approaches one near the center of specimen. Generally, for the next load increment, the index is well above one across the entire width.

In Figure 31 the failure index in the center of the specimen ($s=0.5$) is plotted versus the applied displacement u for all delamination lengths modeled. The failure index for delamination lengths of $a=81.9$ mm, 88.9 mm, and 94.9 mm, were almost identical. For the longer delaminations modeled ($a=101.6$ mm up to 355.6 mm), which are associated with a different global buckling pattern, the index is significantly higher. A different way to visualize the results is to plot the critical displacement, i.e. the applied displacement for $G_T/G_c=1.0$, at the center of the specimen ($s=0.5$) versus the delamination length as shown in Figure 32. The critical displacements for delamination lengths of $a=81.9$ mm, 88.9 mm, and 94.9 mm, were almost identical. For the longer delaminations modeled ($a=101.6$ mm up to 355.6 mm), which are associated with a different global buckling pattern, the critical displacements are significantly lower, which suggests that rapid delamination progress is to be expected once the delamination starts to propagate for a critical applied displacement.

5. SUMMARY AND CONCLUDING REMARKS

The skin/stringer separation of a graphite/epoxy composite panel reinforced with three stringers and subjected to pure shear loading was studied using computational fracture analysis. The shear loading causes the panel to buckle and the resulting out-of-plane deformation initiates skin/stringer separation at the location of an embedded defect. The panel and surrounding load fixture were modeled with shell elements. A small section of the stringer foot and the panel in the vicinity of the embedded defect were modeled with a local 3D solid model. A total of eight delamination lengths were modeled. Across the width of the stringer foot the mixed-mode strain energy release rates were calculated using the virtual crack closure technique. A failure index was calculated by correlating the results with the mixed-mode failure criterion of the graphite/epoxy material.

Initially - for applied loads less than 25% maximum load - the computed failure index is well below one across the entire width of the straight front, which represented the edge of the embedded insert. With loads reaching 35% of the maximum load the failure index approaches one first near one edge of the stringer foot from which the delamination is expected to grow. With increasing modeled delamination length a change in the buckling pattern of the panel is observed locally and globally. The change in the local buckling pattern is believed to be due to stiffness changes caused by the longer delaminations. The different buckling pattern for the longer delaminations caused a change in the distribution of computed failure index across the width of the stringer. For longer delaminations, the failure index was found to be significantly higher which suggests that rapid delamination progress is to be expected once the delamination starts to propagate for a critical applied load.

ACKNOWLEDGEMENTS.

This research was supported by The Boeing Company and the Aviation Applied Technology Directorate under Technology Investment Agreement No. DAAH10-02-2-0001 as part of the Survivable, Affordable, Repairable, Airframe Program (SARAP).

The authors gratefully acknowledge Dr. Dale Berry of ABAQUS[®] Central for providing guidance and help when problems with ABAQUS[®] Standard were encountered during the analyses.

REFERENCES

- [1] I.S. Raju, R. Sistla, and T. Krishnamurthy, *Fracture Mechanics Analyses for Skin-Stiffener Debonding*, Eng. Fracture Mech., vol. 54, pp. 371-385, 1996.
- [2] E.H. Glaessgen, I.S. Raju, and C.C. Poe, *Fracture Mechanics Analysis of Stitched Stiffener-Skin Debonding*, in The 39th AIAA/ASME/ASCE/AHS/ASC Structures, Structural Dynamics and Materials Conference, Long Beach, California, AIAA 98-2022, April 20-23, 1998.
- [3] B.G. Falzon, G.A.O. Davies, and E. Greenhalgh, *Failure of thick-skinned stiffener runout sections loaded in uniaxial compression*, Composite Structures, vol. 53, pp. 223-233, 2001.

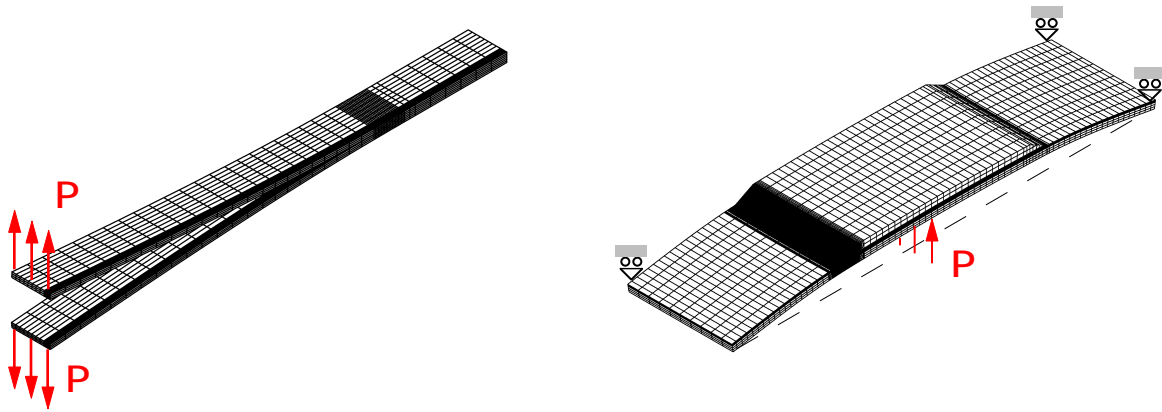
- [4] J.W.H. Yap, M.L. Scott, R.S. Thomson, and D. Hachenberg, *The analysis of skin-to-stiffener debonding in composite aerospace structures*, Composite Structures, vol. 57, pp. 425-435, 2002.
- [5] P.J. Minguet, M.J. Fedro, T.K. O'Brien, R.H. Martin, and L.B. Ilcewicz, *Development of a Structural Test Simulating Pressure Pillowing Effects in Bonded Skin/Stringer/Frame Configuration*, in Proceedings of the Fourth NASA/DoD Advanced Composite Technology Conference, Salt Lake City, Utah, 1993.
- [6] P.J. Minguet and T.K. O'Brien, *Analysis of Composite Skin/Stringer Bond Failures Using a Strain Energy Release Rate Approach*, in The Tenth International Conference on Composite Materials, vol. I, A. Poursartip and K. Street, Eds., pp. 245-252, 1995
- [7] P.J. Minguet and T.K. O'Brien, *Analysis of Test Methods for Characterizing Skin/Stringer Debonding Failures in Reinforced Composite Panels*, in Composite Materials: Testing and Design (Twelfth Volume), ASTM STP 1274, pp. 105-124, 1996
- [8] P.J. Minguet, *Analysis of the Strength of the Interface Between Frame and Skin in a Bonded Composite Fuselage Panel*, in The 38rd AIAA/ASME/ASCE/AHS/ASC Structures, Structural Dynamics and Materials Conference, pp. 2783-2790, 1997
- [9] R. Krueger, M.K. Cvitkovich, T.K. O'Brien, and P.J. Minguet, *Testing and Analysis of Composite Skin/Stringer Debonding Under Multi-Axial Loading*, Journal of Composite Materials, vol. 34, pp. 1263-1300, 2000.
- [10] R. Krueger, I.L. Paris, T.K. O'Brien, and P.J. Minguet, *Fatigue Life Methodology for Bonded Composite Skin/Stringer Configurations*, Journal of Composites Technology and Research, vol. 24, pp. 56-79, 2002.
- [11] T.K. O'Brien, *Fracture Mechanics of Composite Delamination*, in ASM Handbook, Volume 21, Composites: ASM International, pp. 241-245, 2001.
- [12] R.H. Martin, *Incorporating interlaminar fracture mechanics into design*, in International Conference on Designing Cost-Effective Composites: IMechE Conference Transactions, London, U.K., pp. 83-92, 1998.
- [13] R. Krueger and T.K. O'Brien, *A Shell/3D Modeling Technique for the Analysis of Delaminated Composite Laminates*, NASA/TM-2000-210287, ARL-TR-2207, 2000.
- [14] *ASTM D 5528-94a, Standard Test Method for Mode I Interlaminar Fracture Toughness of Unidirectional Fiber-Reinforced Polymer Matrix Composites*, in Annual Book of ASTM Standards, vol. 15.03: American Society for Testing and Materials, 2000.
- [15] R.H. Martin and B.D. Davidson, *Mode II Fracture Toughness Evaluation Using A Four Point Bend End Notched Flexure Test*, Plastics, Rubber and Composites, vol. 28, pp. 401-406, 1999.
- [16] M.L. Benzeggagh and M. Kenane, *Measurement of mixed-mode delamination fracture toughness of unidirectional glass/epoxy composites with mixed-mode bending apparatus*, Composites Science and Technology, vol. 56, pp. 439-449, 1996.
- [17] R.H. Martin, *Evaluation of the Split Cantilever Beam for Mode III Delamination Testing*, in Composite Materials: Fatigue and Fracture (Third Volume), ASTM STP 1110, pp. 243-266, 1991.
- [18] S.M. Lee, *An Edge Crack Torsion Method for Mode III Delamination Fracture Testing*, J. of Composite Technology and Research., pp. 193--201, 1993.
- [19] P. Robinson and D.Q. Song, *A new Mode III delamination test for composites*, Advanced Composites Letters, vol. 1, pp. 160--164, 1992.

- [20] J. Li, S.M. Lee, E.W. Lee, and T.K. O'Brien, *Evaluation of the Edge Crack Torsion ECT Test for Mode III Interlaminar Fracture Toughness of Laminated Composites*, Journal of Composites Technology and Research, vol. 19, pp. 174-183, 1997.
- [21] J.G. Ratcliffe, *Characterization of the Edge Crack Torsion (ECT) Test for Mode III Fracture Toughness Measurement of Laminated Composites*, NASA/TM-2004-213269, 2004.
- [22] E.F. Rybicki and M.F. Kanninen, *A Finite Element Calculation of Stress Intensity Factors by a Modified Crack Closure Integral*, Eng. Fracture Mech., vol. 9, pp. 931-938, 1977.
- [23] R. Krueger, *Virtual Crack Closure Technique: History, Approach and Applications*, Applied Mechanics Reviews, vol. 57, pp. 109-143, 2004.
- [24] E.H. Glaessgen, W.T. Riddell, and I.S. Raju, *Effect of Shear Deformation and Continuity on Delamination Modeling with Plate Elements*, in The 39th AIAA/ASME/ASCE/AHS/ASC Structures, Structural Dynamics and Materials Conference, 1998.
- [25] E.H. Glaessgen, W.T. Riddell, and I.S. Raju, *Nodal Constraint, Shear Deformation and Continuity Effects Related to the Modeling of Debonding of Laminates, Using Plate Elements*, CMES, vol. 3, pp. 103-116, 2002.
- [26] J.T. Wang and I.S. Raju, *Strain energy release rate formulae for skin-stiffener debond modeled with plate elements*, Engineering Fracture Mechanics, vol. 54, pp. 211-228, 1996.
- [27] R. Krueger and T.K. O'Brien, *A Shell/3D Modeling Technique for the Analysis of Delaminated Composite Laminates*, Composites Part A: Applied Science and Manufacturing, vol. 32, pp. 25-44, 2001.
- [28] R. Krueger and P.J. Minguet, *Analysis of Composite Skin-Stiffener Debond Specimens Using a Shell/3D Modeling Technique and Submodeling*, Hampton, VA, NIA Report No. 2004-04, NASA/CR-2004-212684, 2004.
- [29] R. Krueger and P.J. Minguet, *Analysis of Composite Skin-stiffener Debond Specimens Using Volume Elements and a Shell/3D Modeling Technique*, NASA/CR-2002-211947, ICASE Report No. 2002-38, 2002.
- [30] P. Minguet, *Boeing SARAP Status Report - Durability (2nd Quarter 2002)*, 2002.

Table 1.
Material Properties

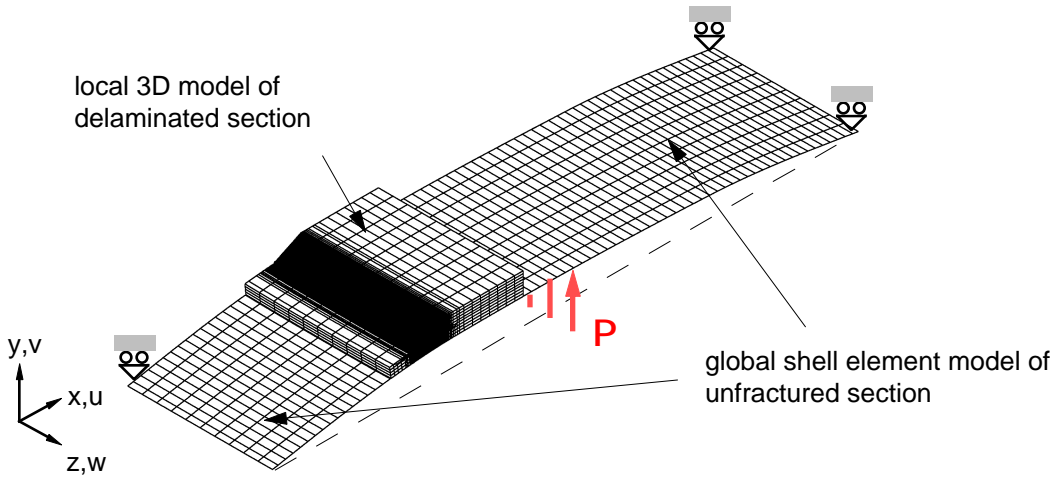
IM7/8552 Unidirectional Graphite/Epoxy Prepreg		
$E_{11} = 161.0 \text{ GPa}$	$E_{22} = 11.38 \text{ GPa}$	$E_{33} = 11.38 \text{ GPa}$
$\nu_{12} = 0.32$	$\nu_{13} = 0.32$	$\nu_{23} = 0.45$
$G_{12} = 5.17 \text{ GPa}$	$G_{13} = 5.17 \text{ GPa}$	$G_{23} = 3.92 \text{ GPa}$
IM7/8552 Graphite/Epoxy Plain Weave Fabric		
$E_{11} = 71.7 \text{ GPa}$	$E_{22} = 71.7 \text{ GPa}$	$E_{33} = 10.3 \text{ GPa}$
$\nu_{12} = 0.04$	$\nu_{13} = 0.35$	$\nu_{23} = 0.35$
$G_{12} = 4.48 \text{ GPa}$	$G_{13} = 4.14 \text{ GPa}$	$G_{23} = 4.14 \text{ GPa}$
Grade 5 FM300 Adhesive		
$E = 1.72 \text{ GPa}$	$\nu = 0.3$	(assumed isotropic)

The material properties are given with reference to the ply coordinate axes where index 11 denotes the ply principal axis that coincides with the direction of maximum in-plane Young's modulus (fiber direction). Index 22 denotes the direction transverse to the fiber in the plane of the lamina and index 33 the direction perpendicular to the plane of the lamina.

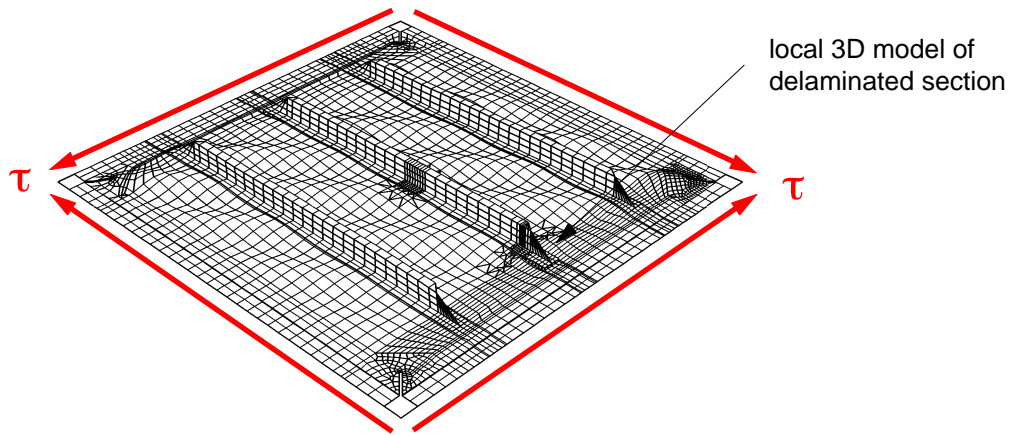


(a) Deformed 3D model of half a DCB specimen (250 mm x 12.5 mm).

(b) Deformed 3D model of a skin/stringer specimen (101.6 mm x 25.4 mm) [28,29].



(c) Deformed shell/3D model of a skin/stringer specimen (101.6 mm x 25.4 mm) [28,29].



(d) Deformed shell model of stringer stiffened panel under shear loading (1016 mm x 1016 mm).

Figure 1. Finite element analyses of different complexity.

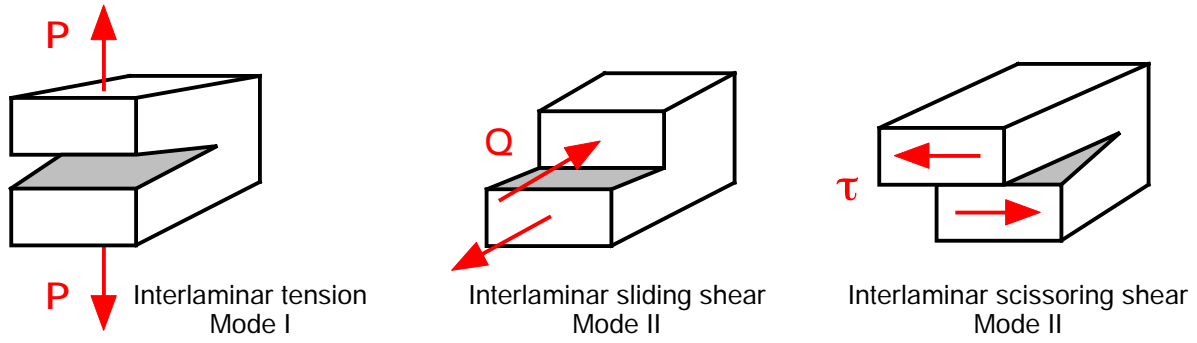


Figure 2: Fracture Modes.

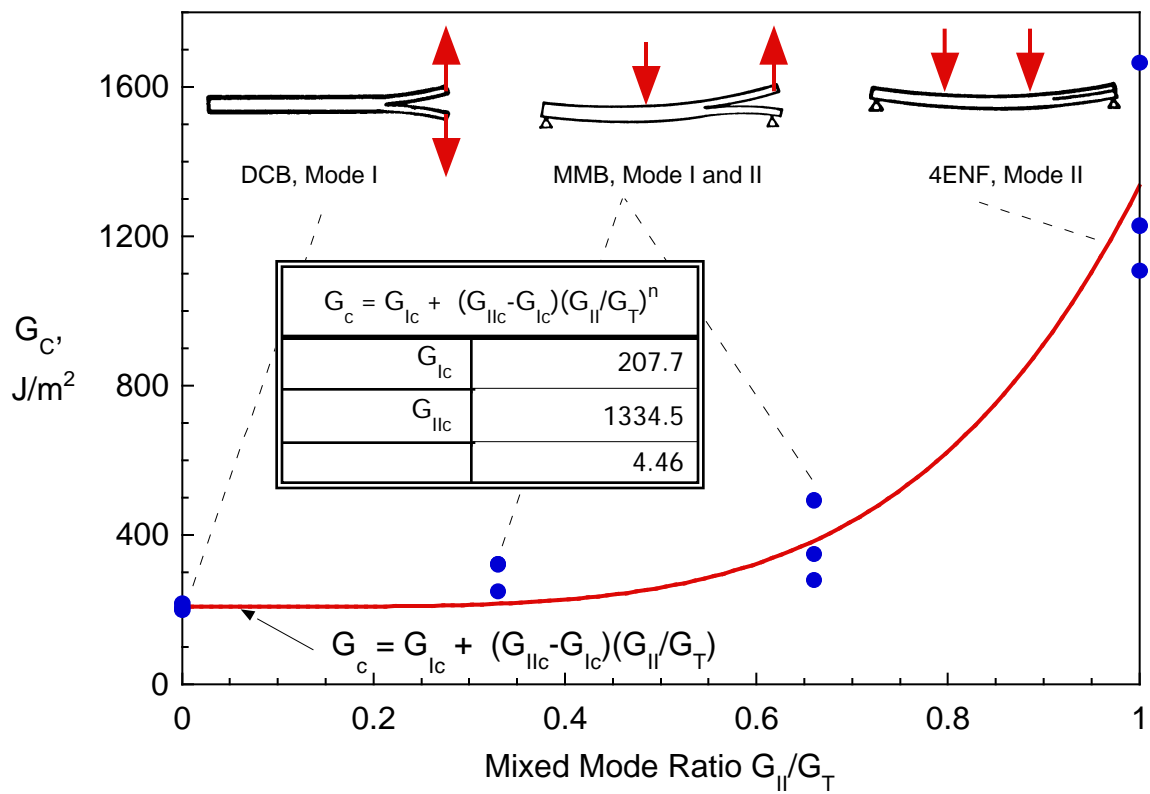
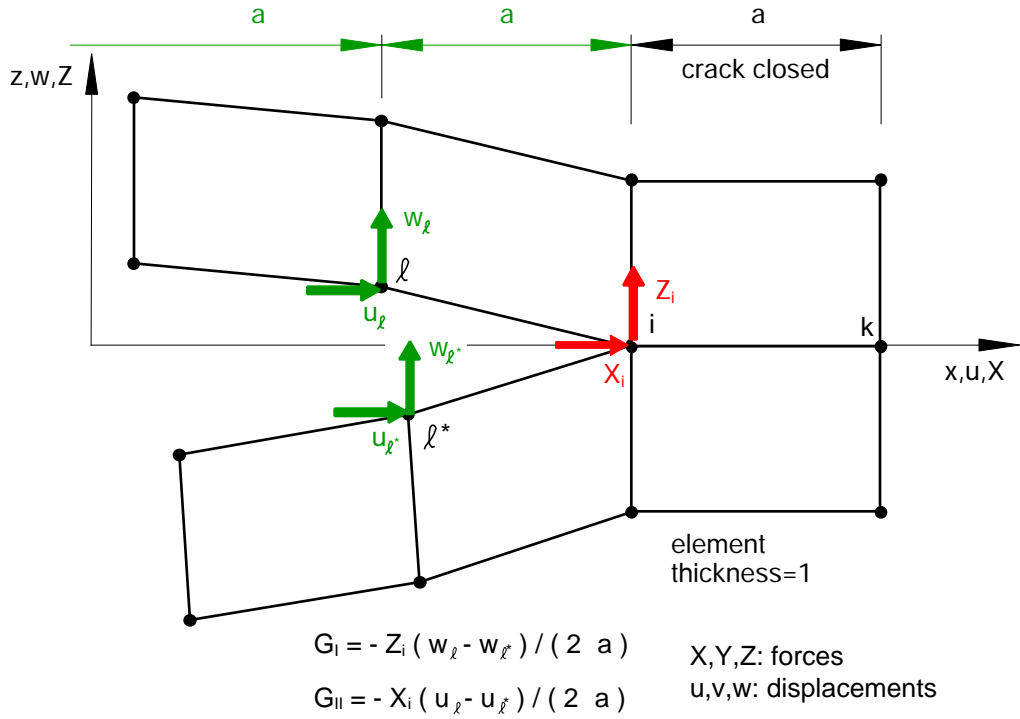
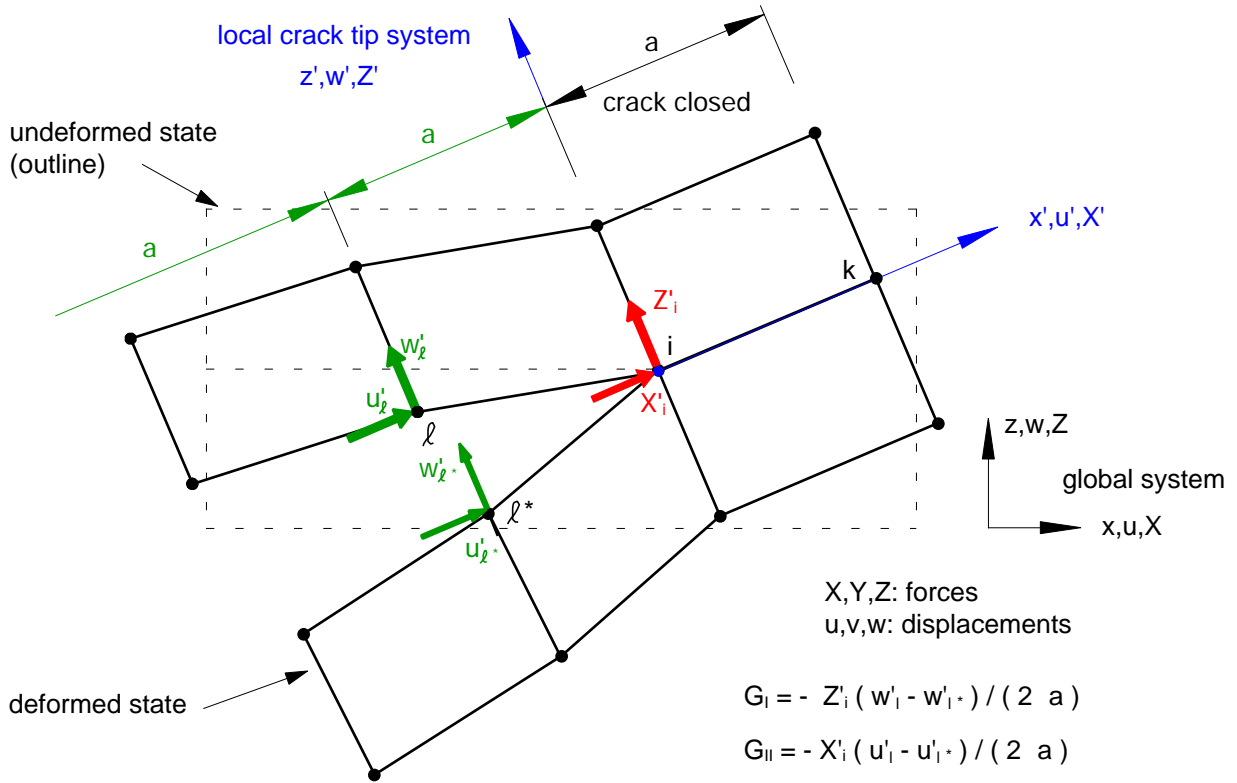


Figure 3: Mixed-mode fracture criterion for IM7/8552.

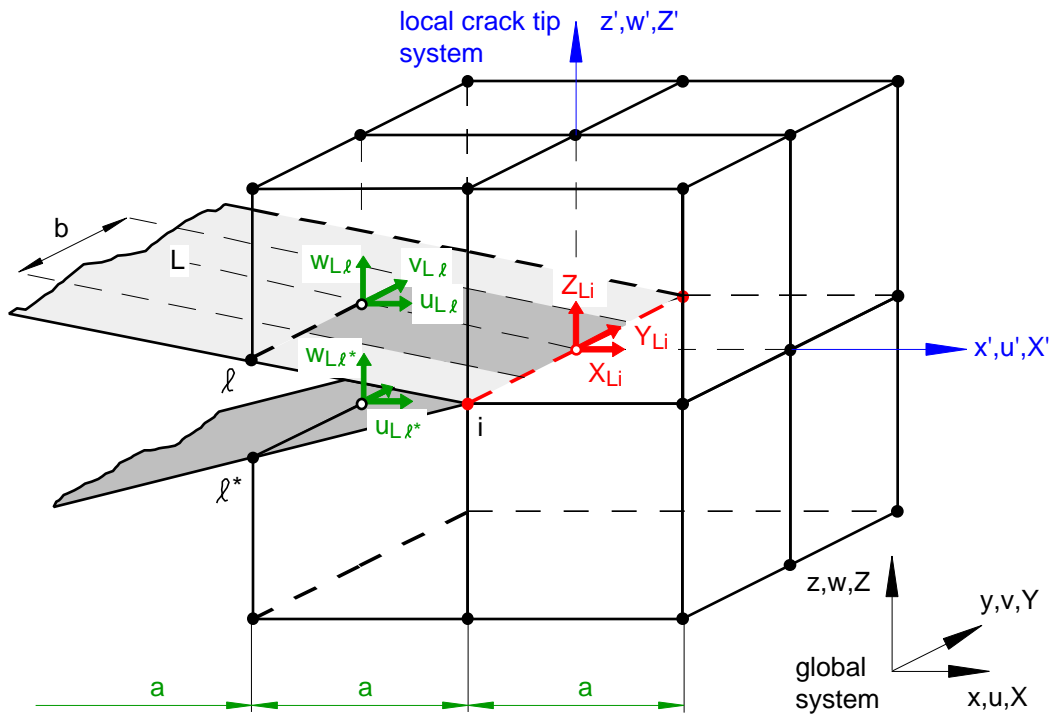


(a): Virtual Crack Closure Technique (VCCT) for four-noded element.

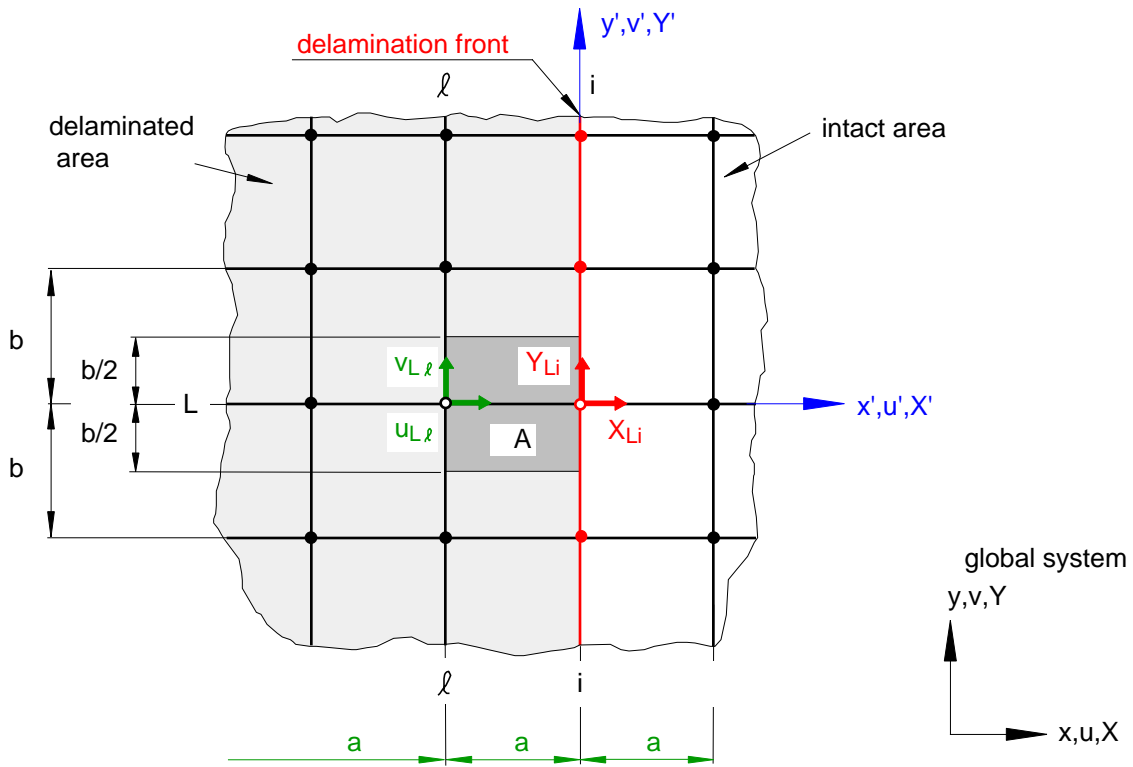


(b): Virtual Crack Closure Technique (VCCT) for geometrically nonlinear analysis.

Figure 4: Virtual Crack Closure Technique for two-dimensional analysis

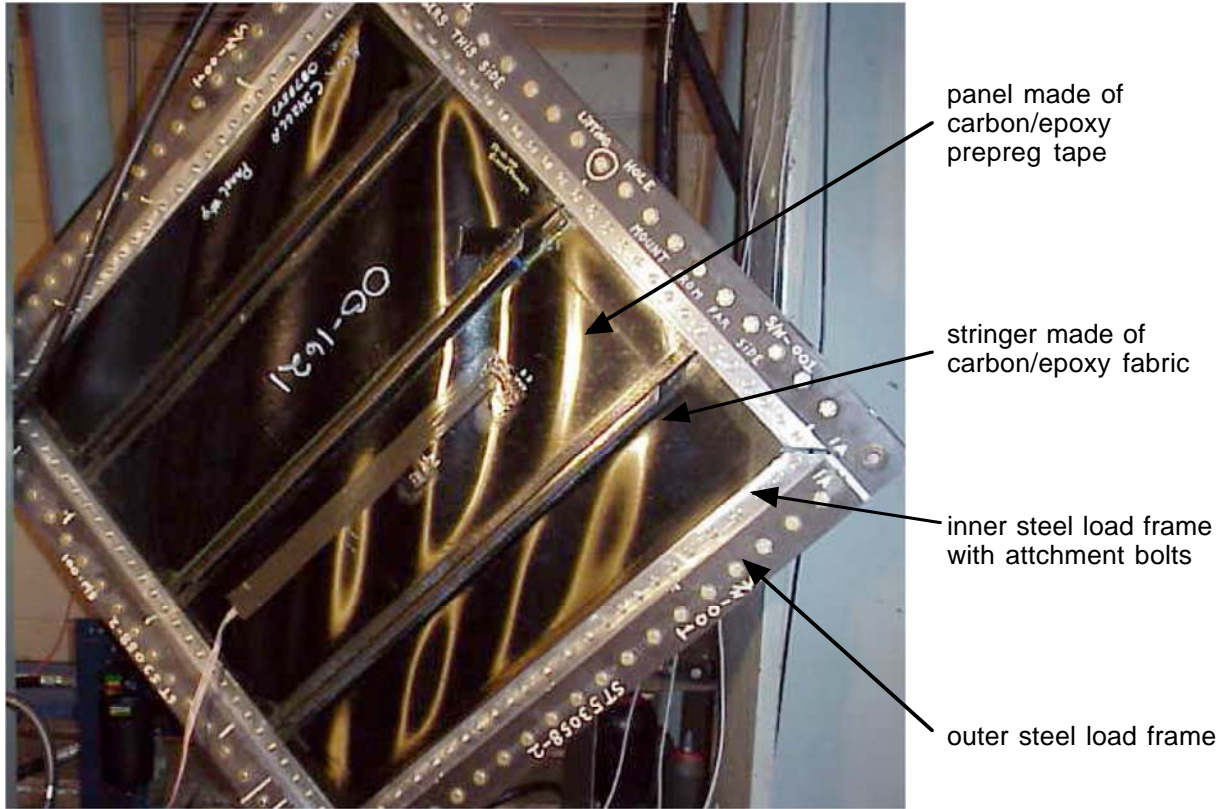


(a). 3D view

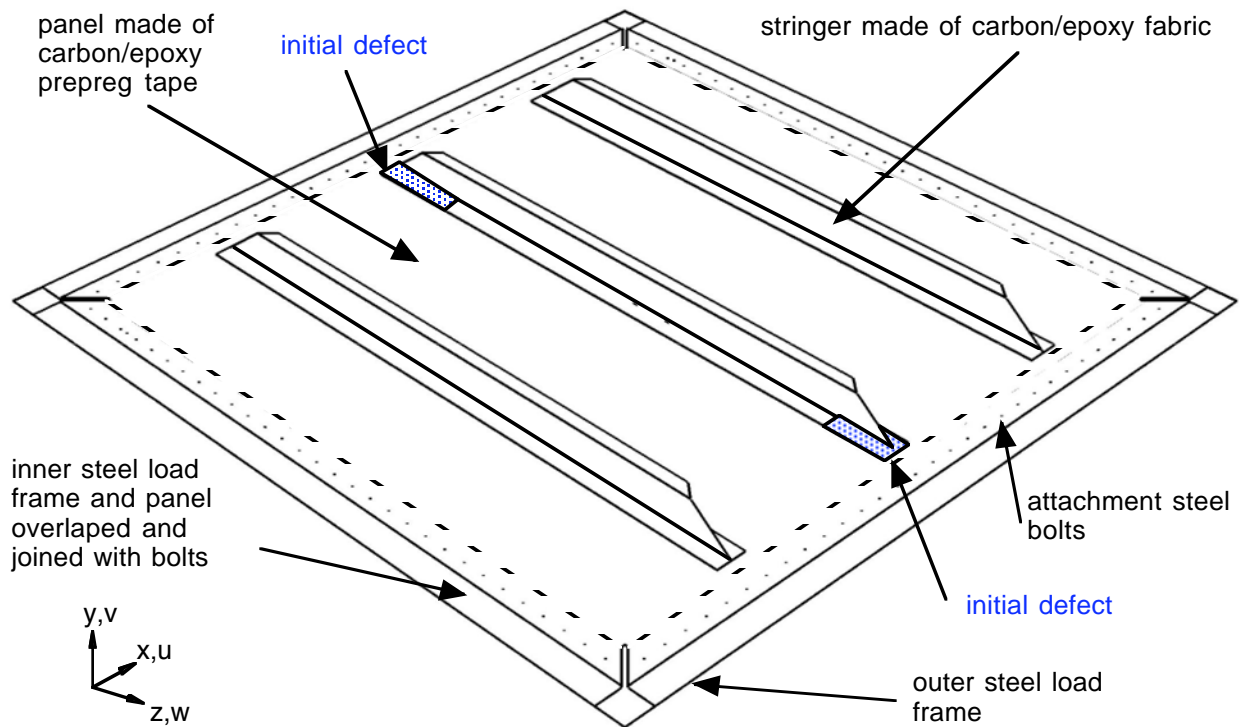


(b). Top view of upper surface (lower surface terms are omitted for clarity)

Figure 5. Virtual Crack Closure Technique for eight noded solid elements.

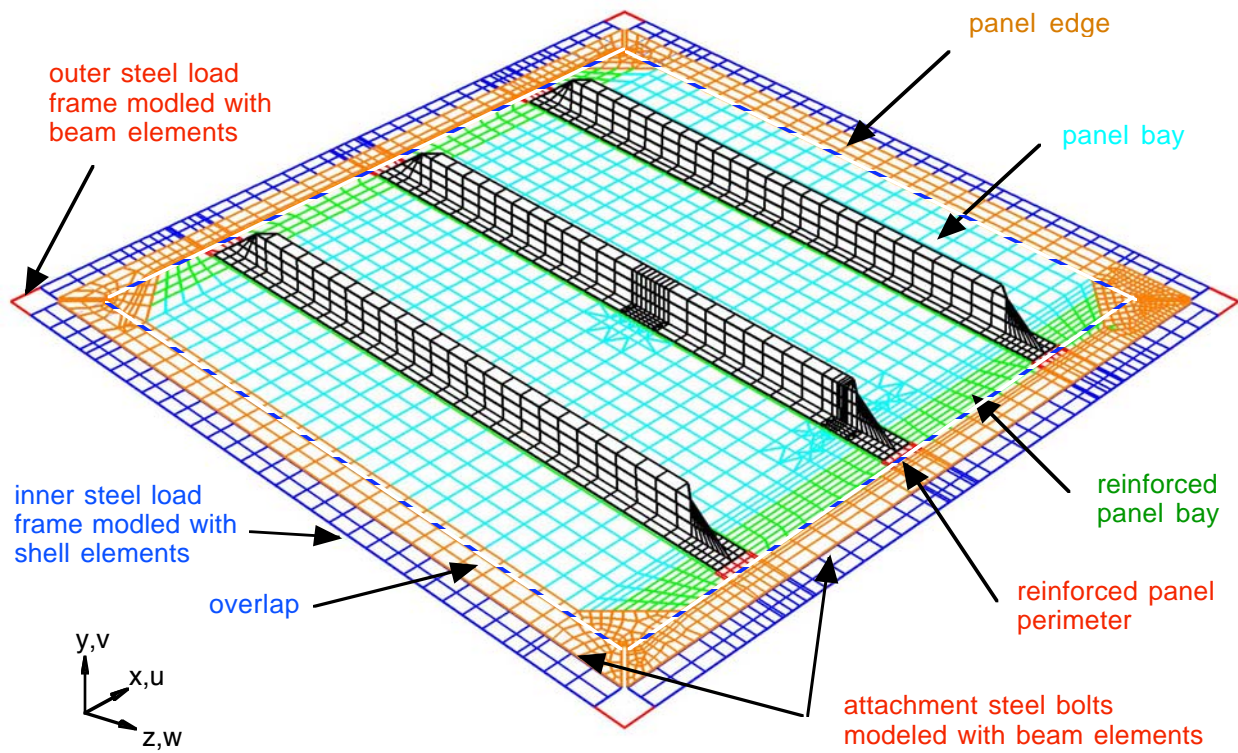


a. Buckled composite panel under shear loading with picture frame

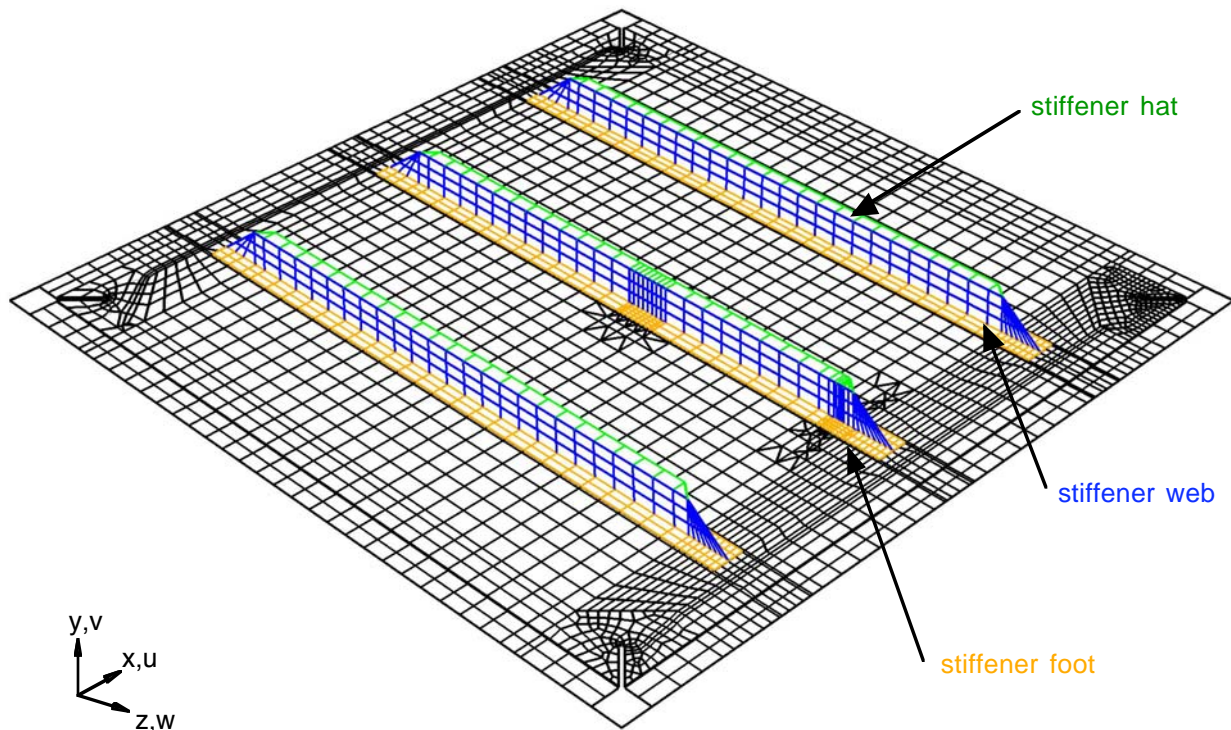


b. Outline of composite panel and steel load frame

Figure 6. Stringer stiffened composite panel (1016 mm x 1016 mm)



a. Composite panel and load frame components



b. Stiffener components

Figure 7. Finite element model of stringer stiffened composite panel and load frame

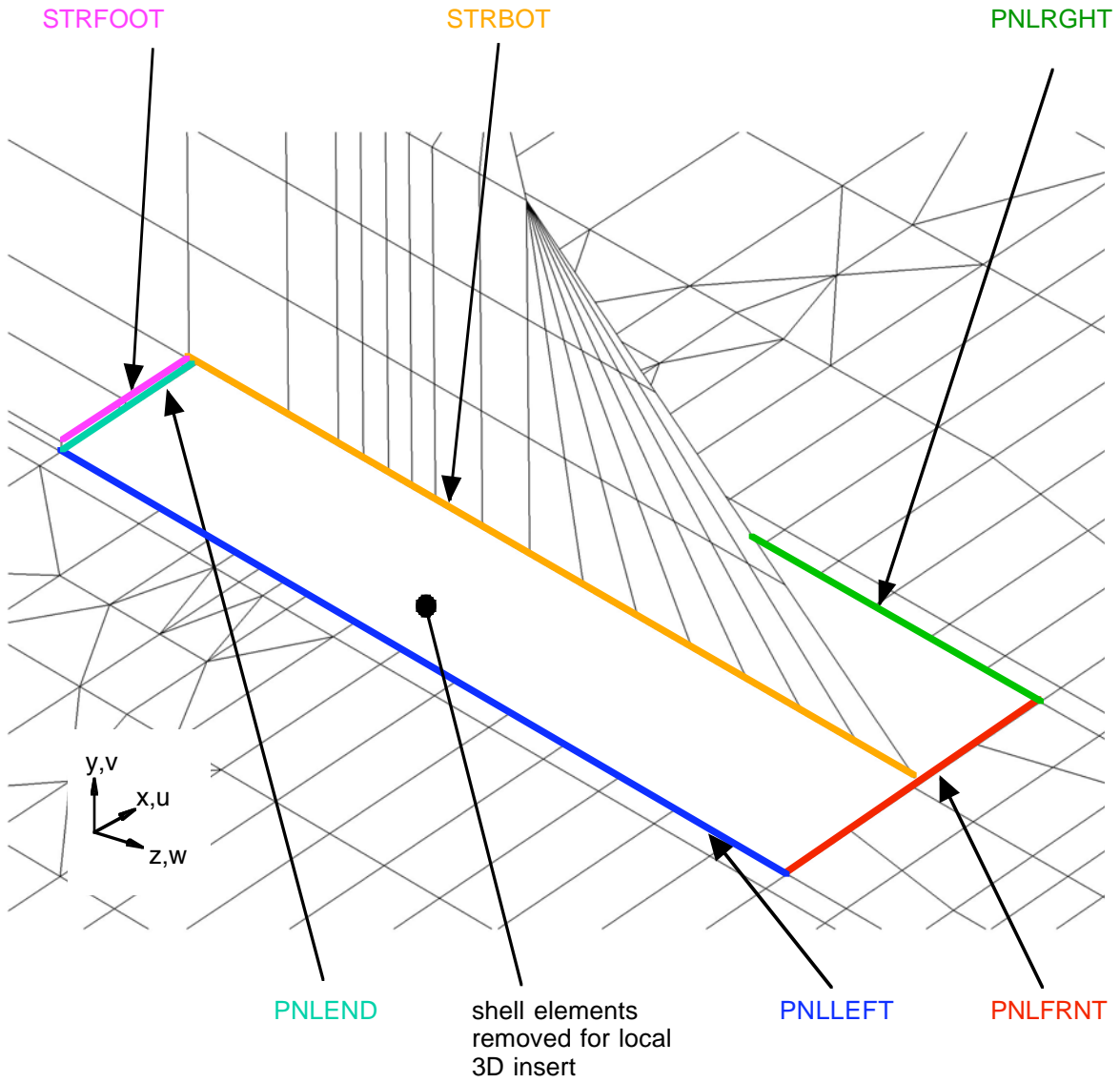
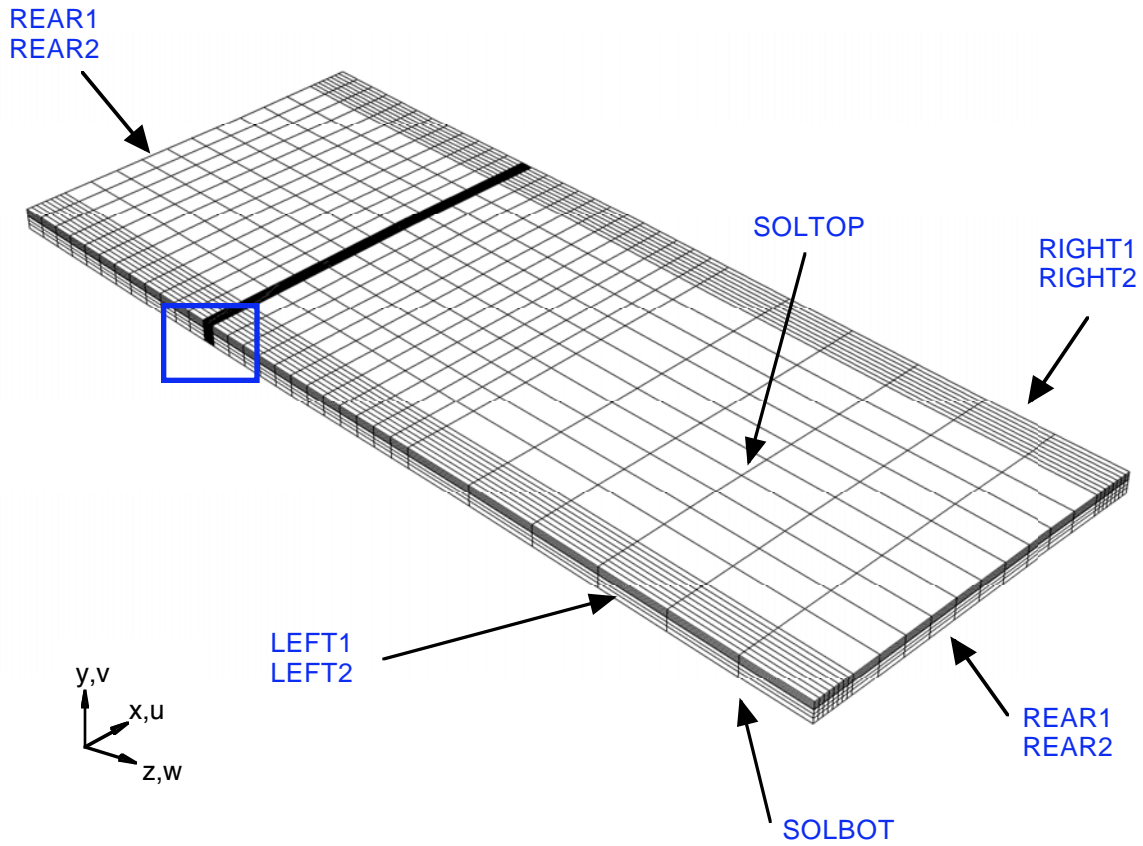
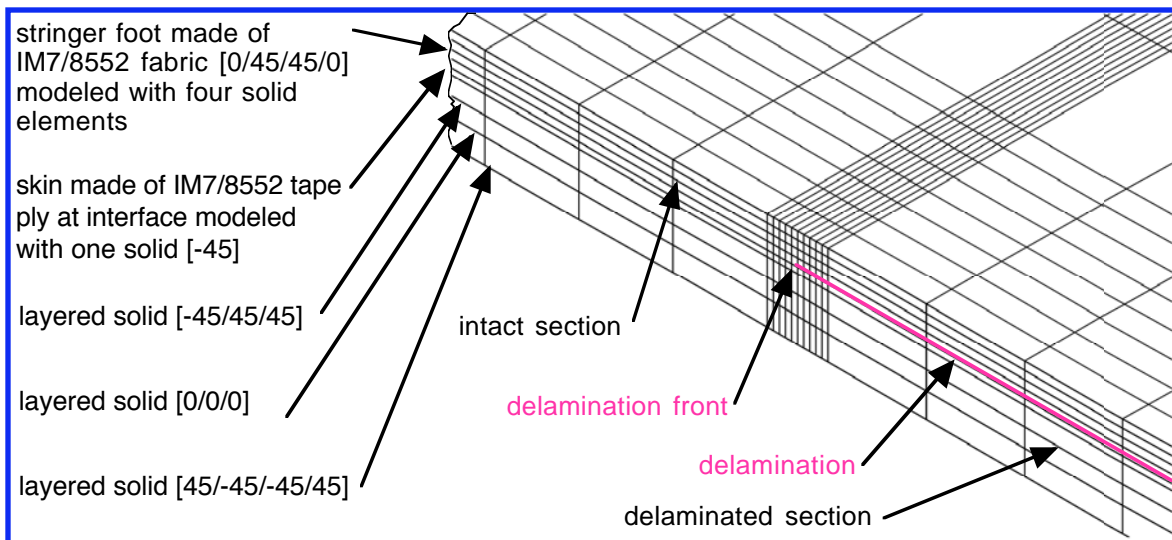


Figure 9. Detail of global shell model with edges for shell to solid coupling

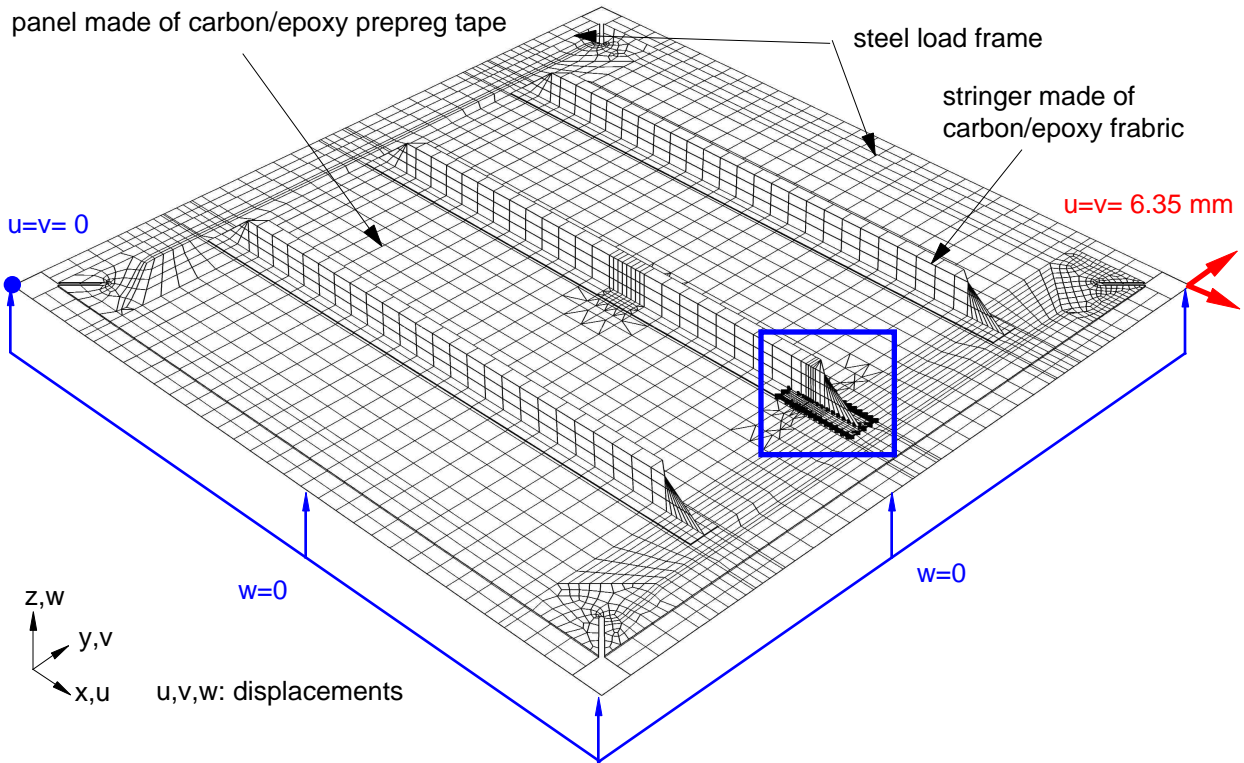


a. Local 3D insert model and surfaces for shell to solid coupling

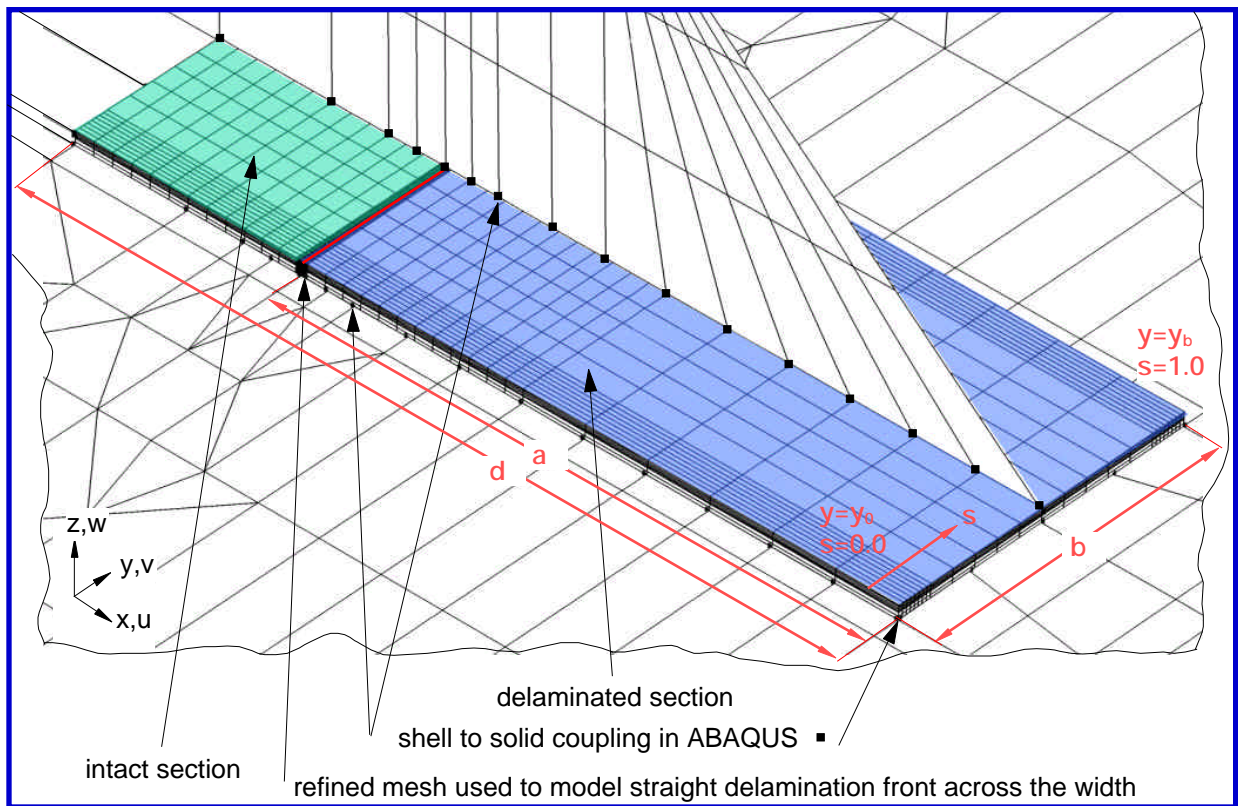


b. Detail of local 3D insert model around delamination front

Figure 10: Local insert model

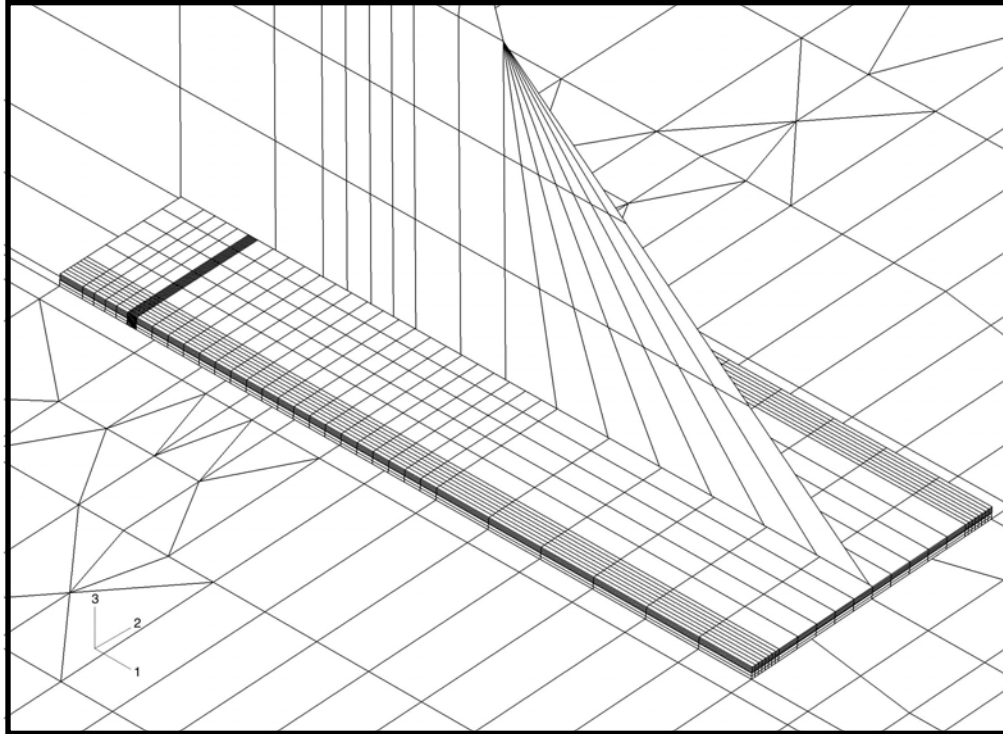


a. Global shell model of panel (1016 mm x 1016 mm) and load frame

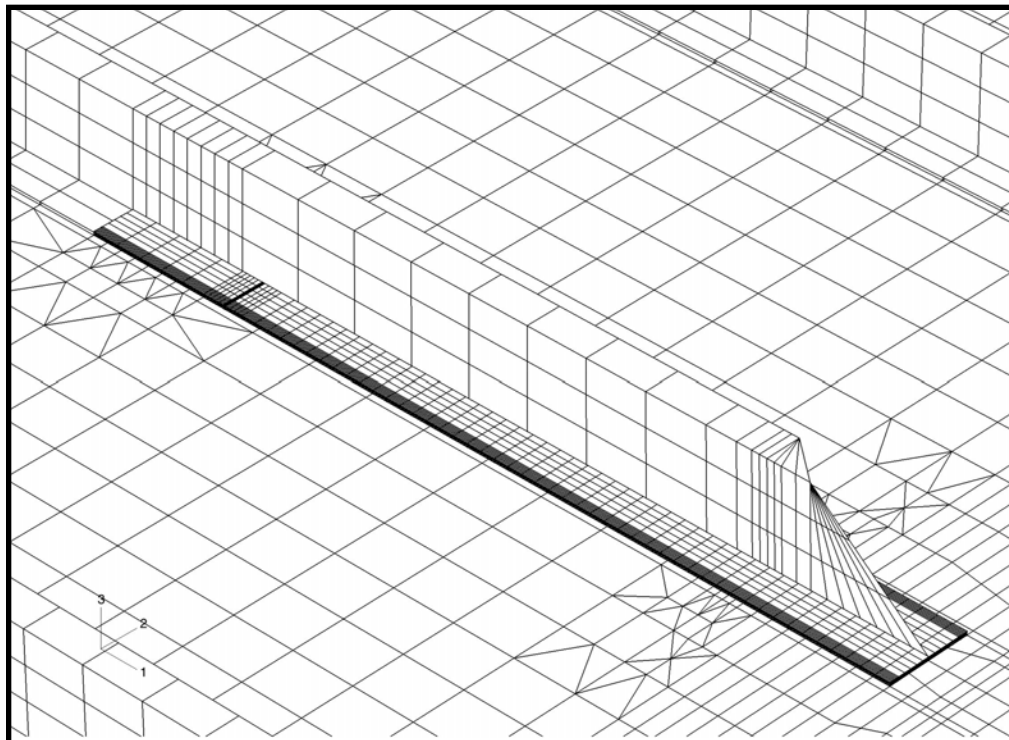


b. Detail of center stringer with local 3D insert

Figure 11: Shell model of stiffened panel with detail of local 3D insert

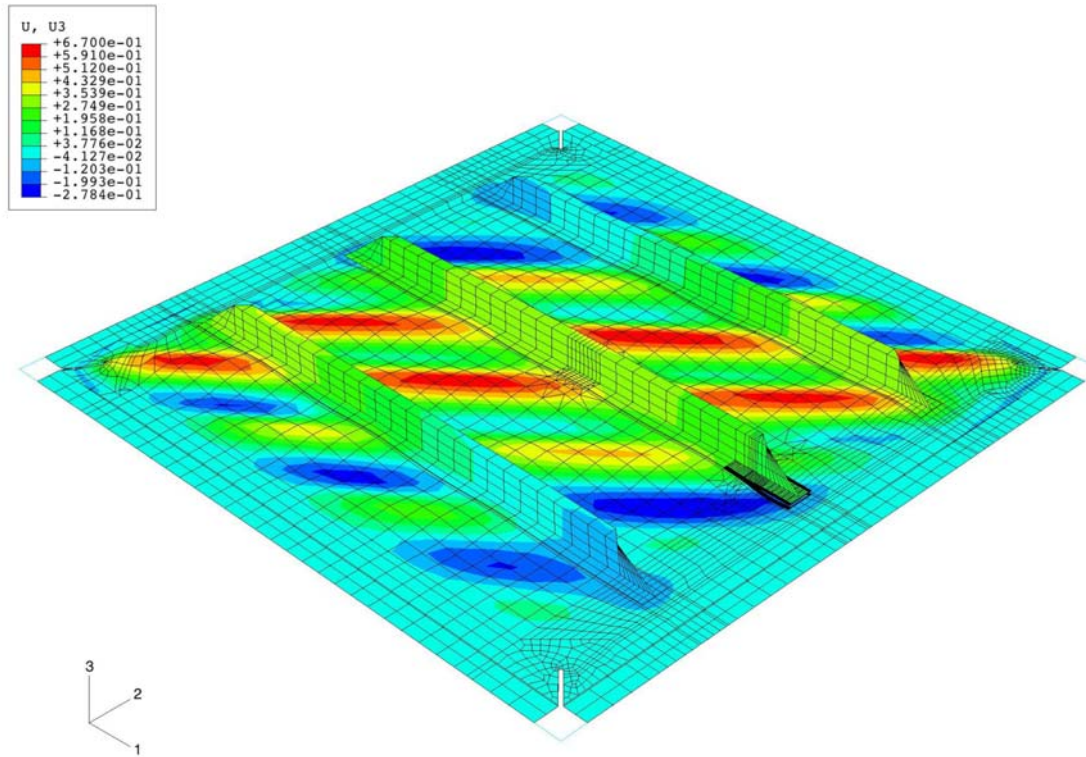


a. Short local 3D insert ($c=116.7$ mm) with $a=101.6$ mm delamination length

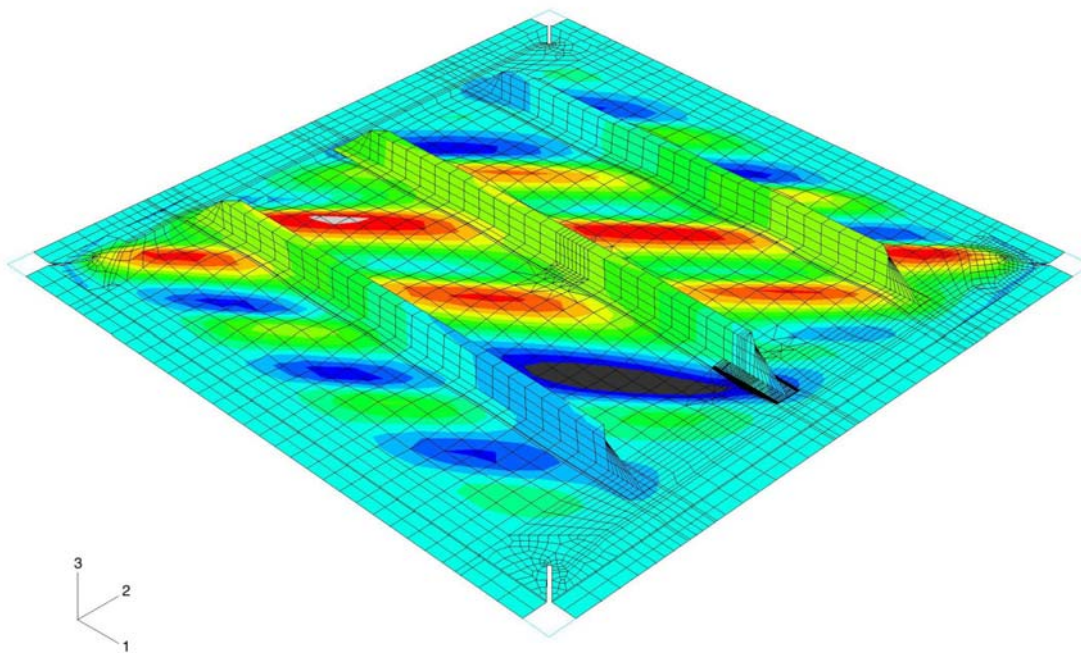


b. Long local 3D insert ($c=431.2$ mm) with $a=355.6$ mm delamination length

Figure 12: Local 3D insert models

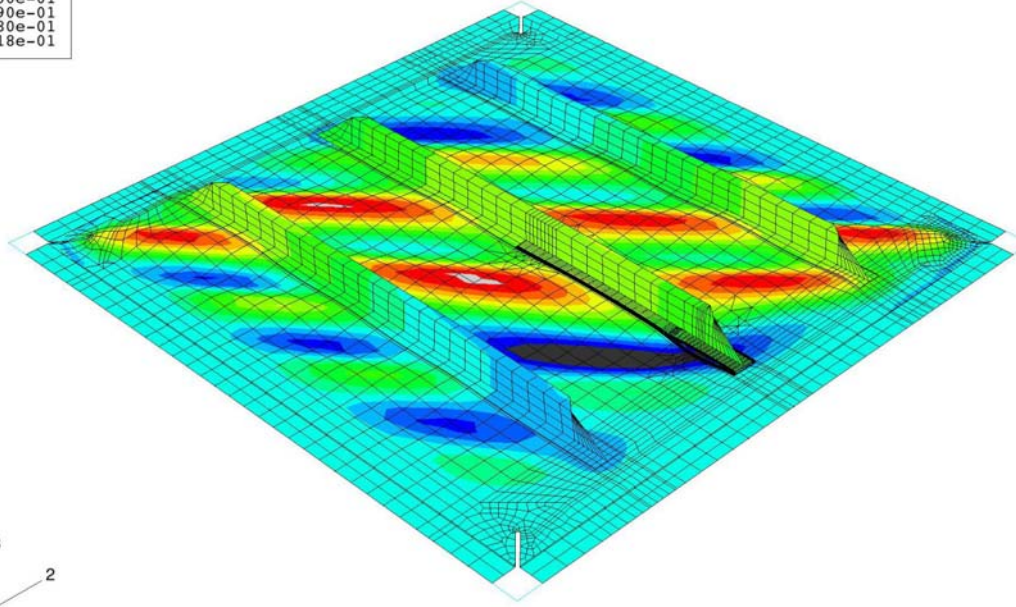
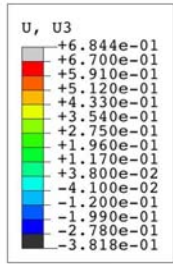


a. Deformed panel for 81.9 mm delamination

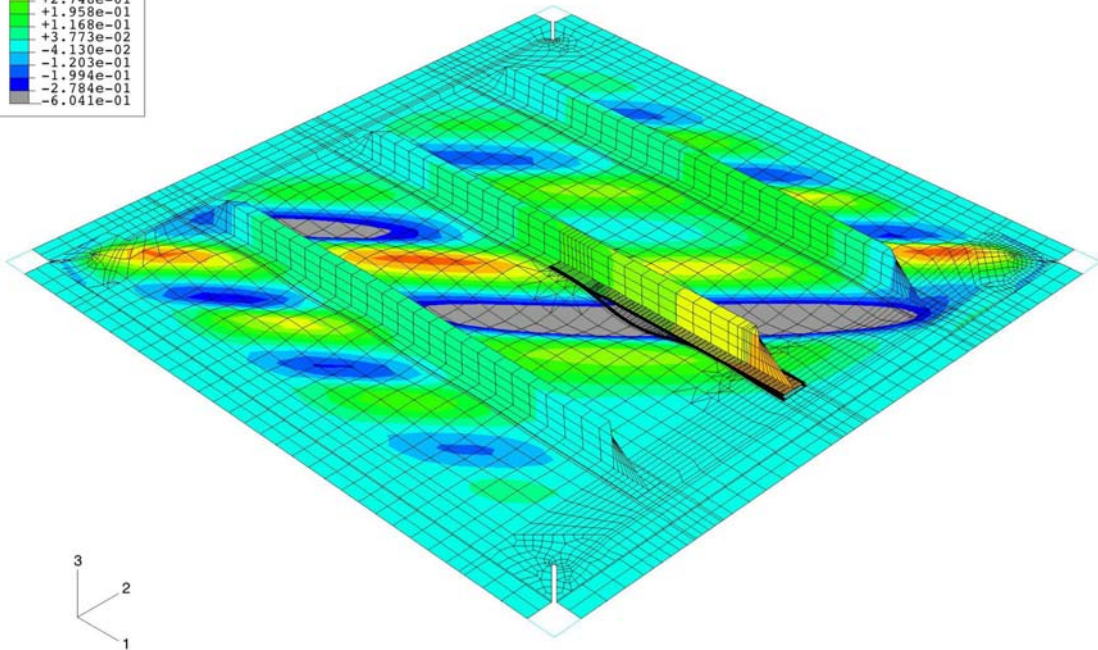
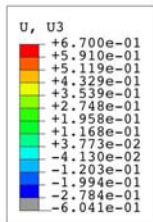


b. Deformed panel for 101.6 mm delamination

Figure 13: Out of plane deformation of stiffened panel with short insert

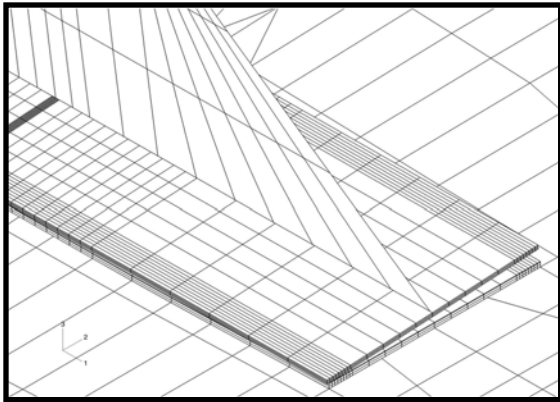


a. Deformed panel for 127.0 mm delamination

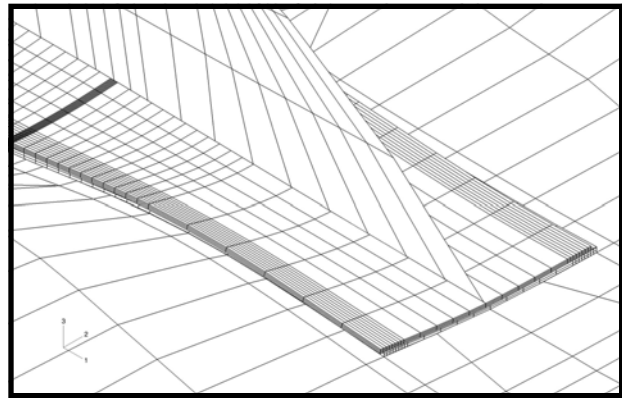


b. Deformed panel for 355.6 mm delamination

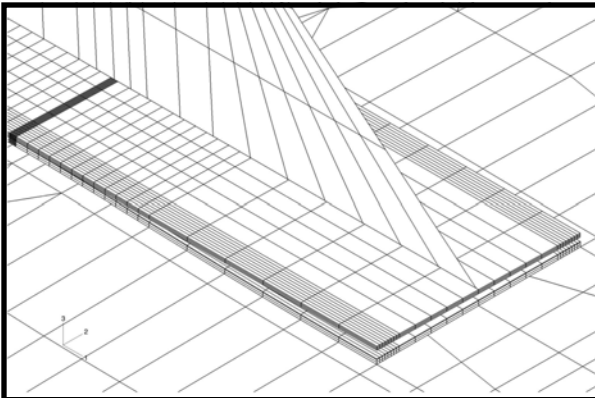
Figure 14: Out of plane deformation of stiffened panel with long insert



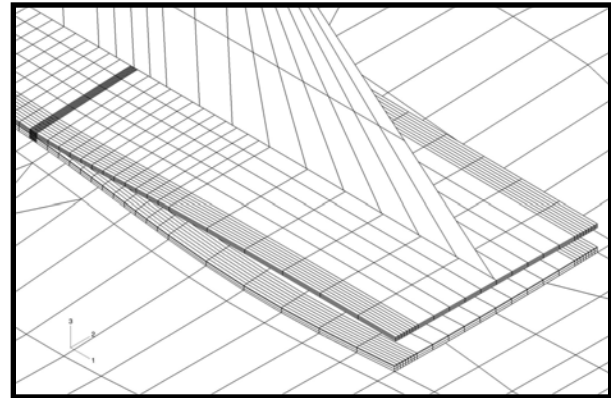
a. Increment 5 (displacement enlarged)



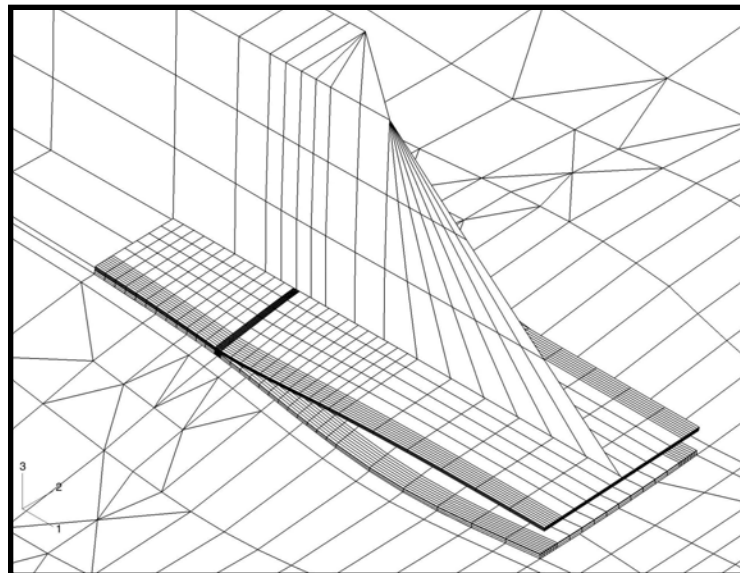
b. Increment 15 (displacement enlarged)



c. Increment 20 (displacement enlarged)

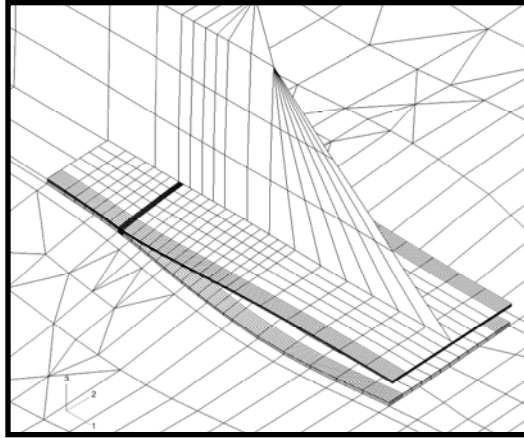


d. Increment 41 (true scale)

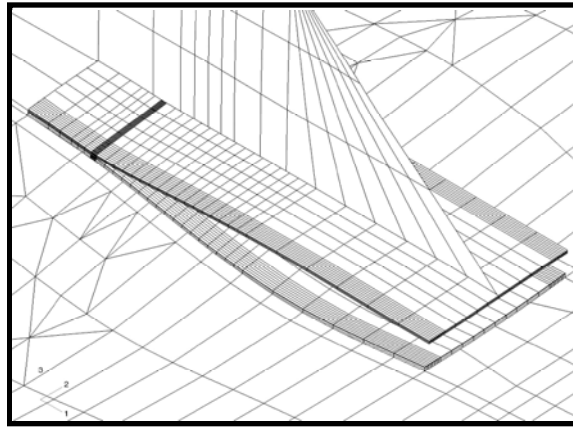


e. Increment 41 (true scale)

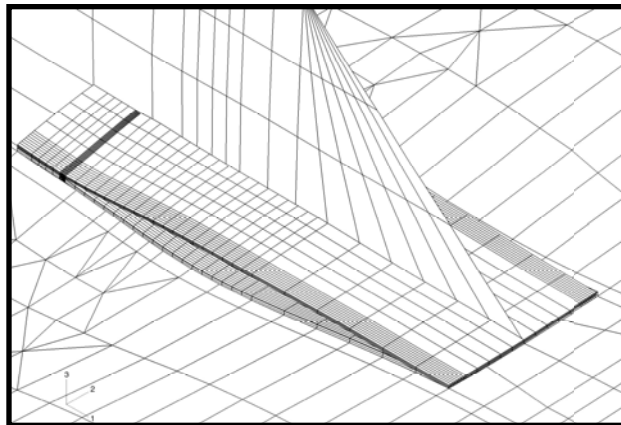
Figure 15: Detail of deformed center stringer with short local 3D insert for 81.9 mm delamination



a. Local 3D insert for 88.9 mm delamination

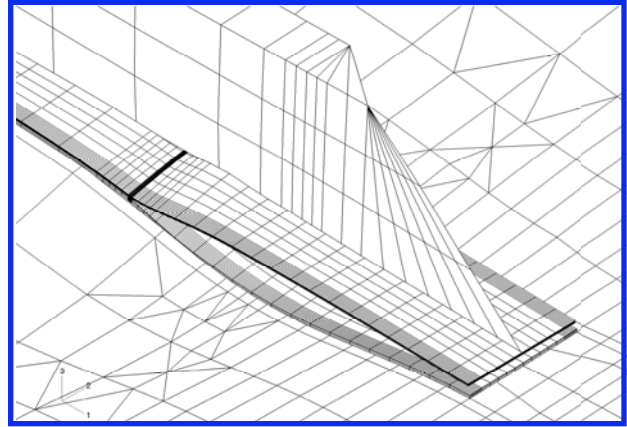
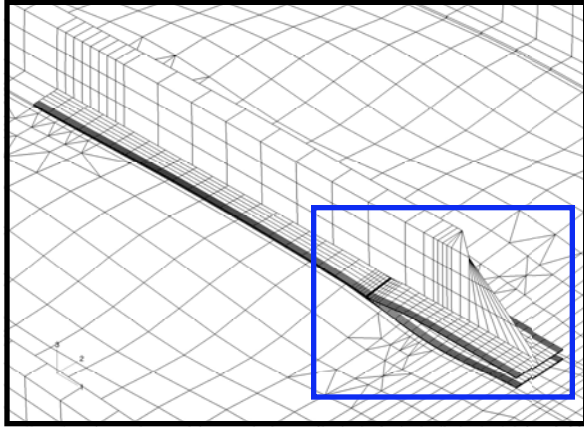


b. Local 3D insert for 94.9 mm delamination

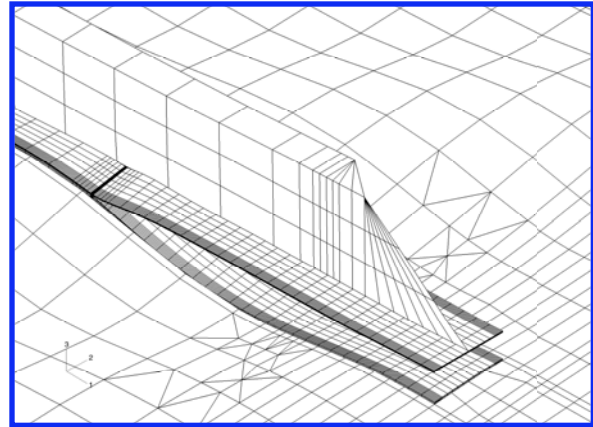
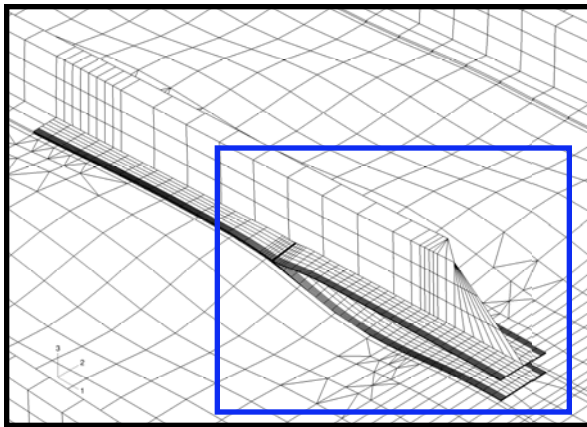


c. Local 3D insert for 101.6 mm delamination

Figure 16: *Detail of deformed center stringer with short local 3D insert.*

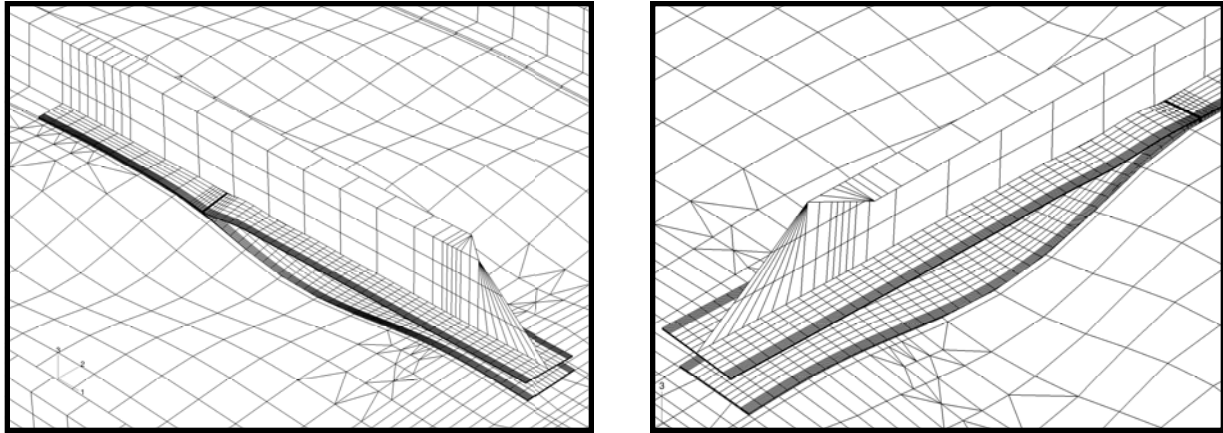


a. Local 3D insert for 127.0 mm delamination length with detail

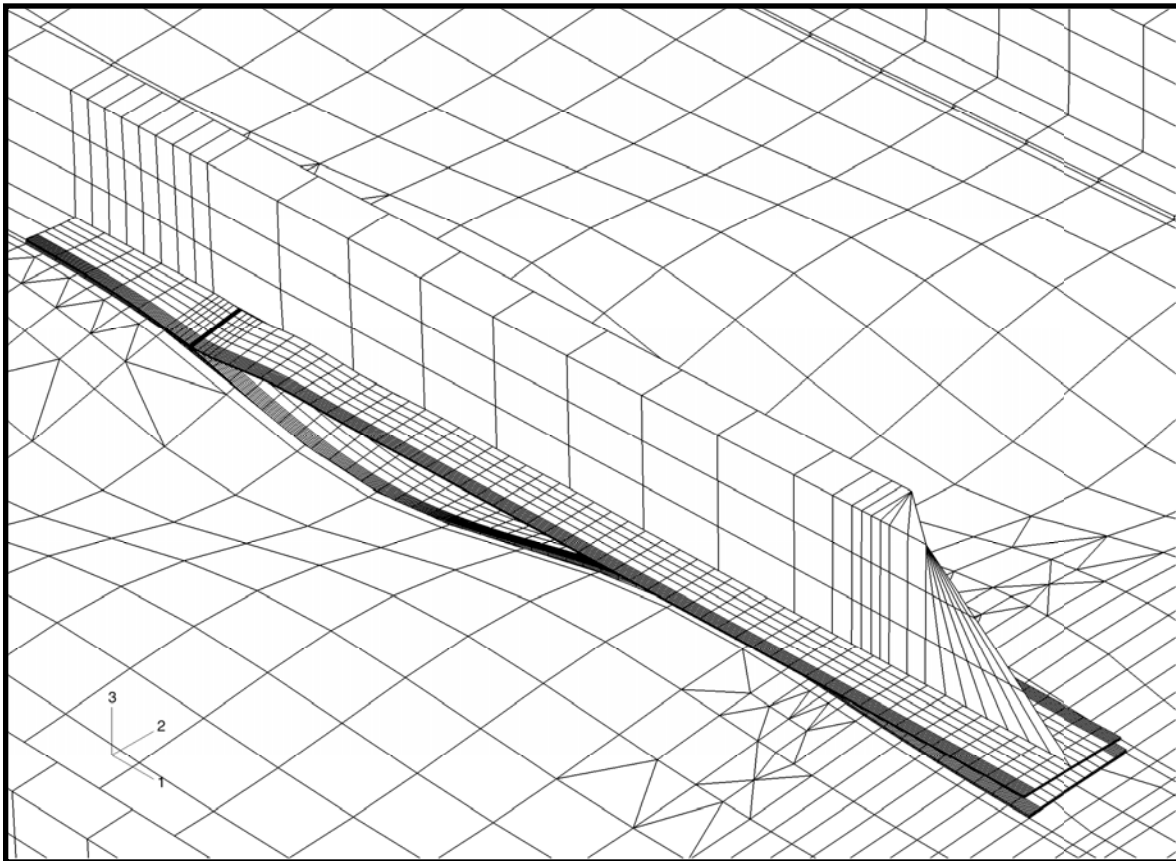


b. Local 3D insert for 203.2 mm delamination length with detail

Figure 17: Detail of deformed center stringer with long local 3D insert.



a. Local 3D insert for 279.4 mm delamination length with detail



b. Local 3D insert for 355.6 mm delamination length with detail

Figure 18: Detail of deformed center stringer with long local 3D insert.

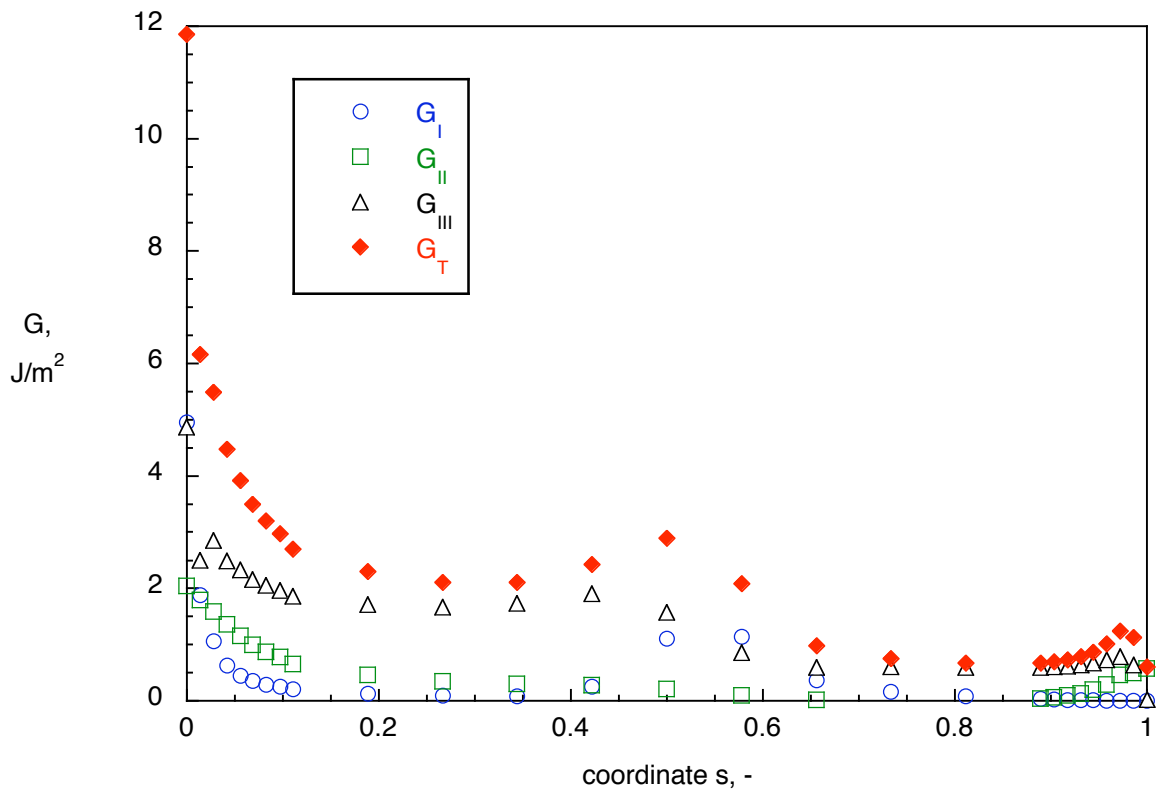


Figure 19. Computed energy release rate across the width of the stringer at increment 5 for delamination length $a=81.9$ mm.

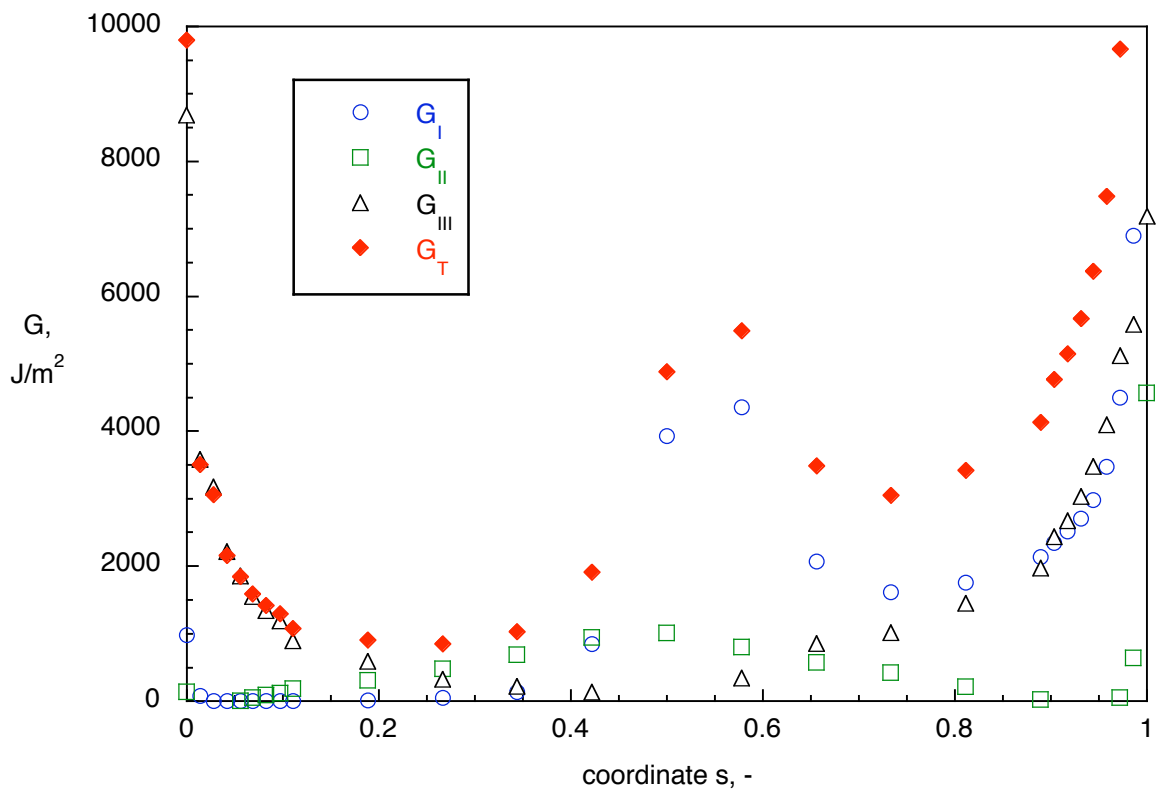


Figure 20. Computed energy release rate across the width of the stringer at increment 41 for delamination length $a=81.9$ mm.

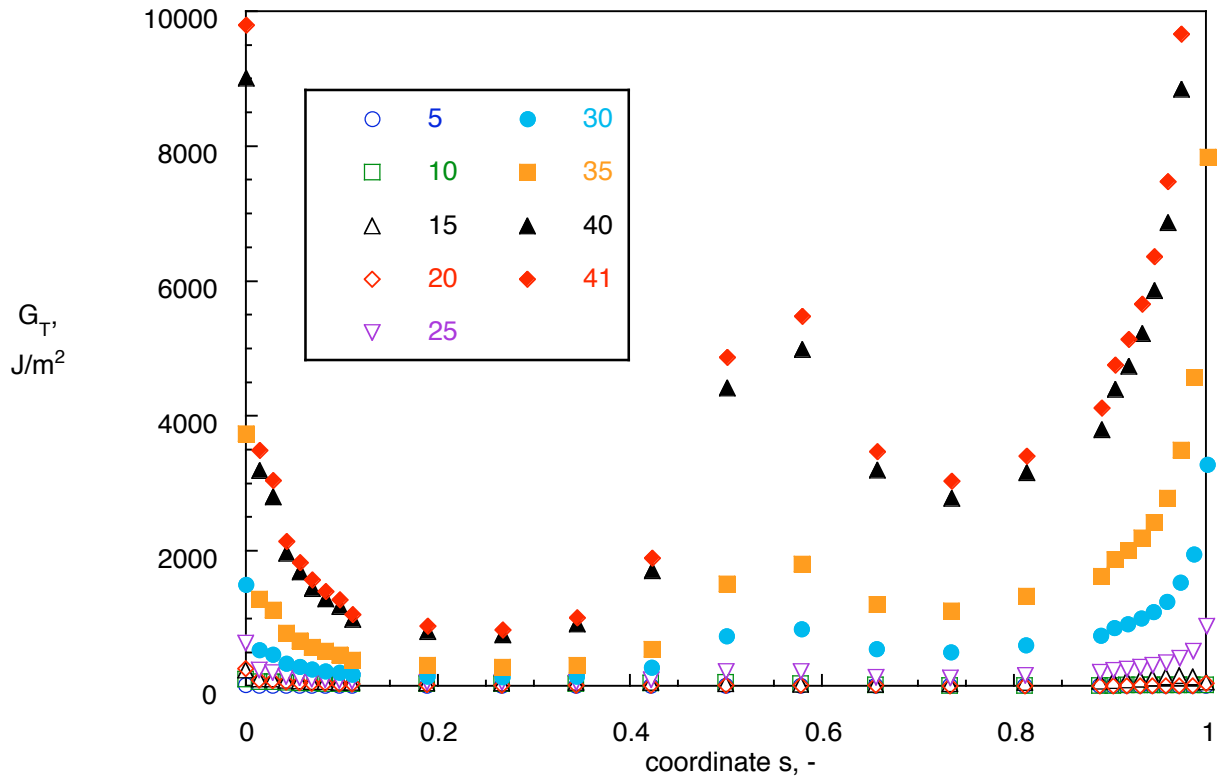


Figure 21. Computed total energy release rate across the width of the stringer for all increments for delamination length $a=81.9$ mm.

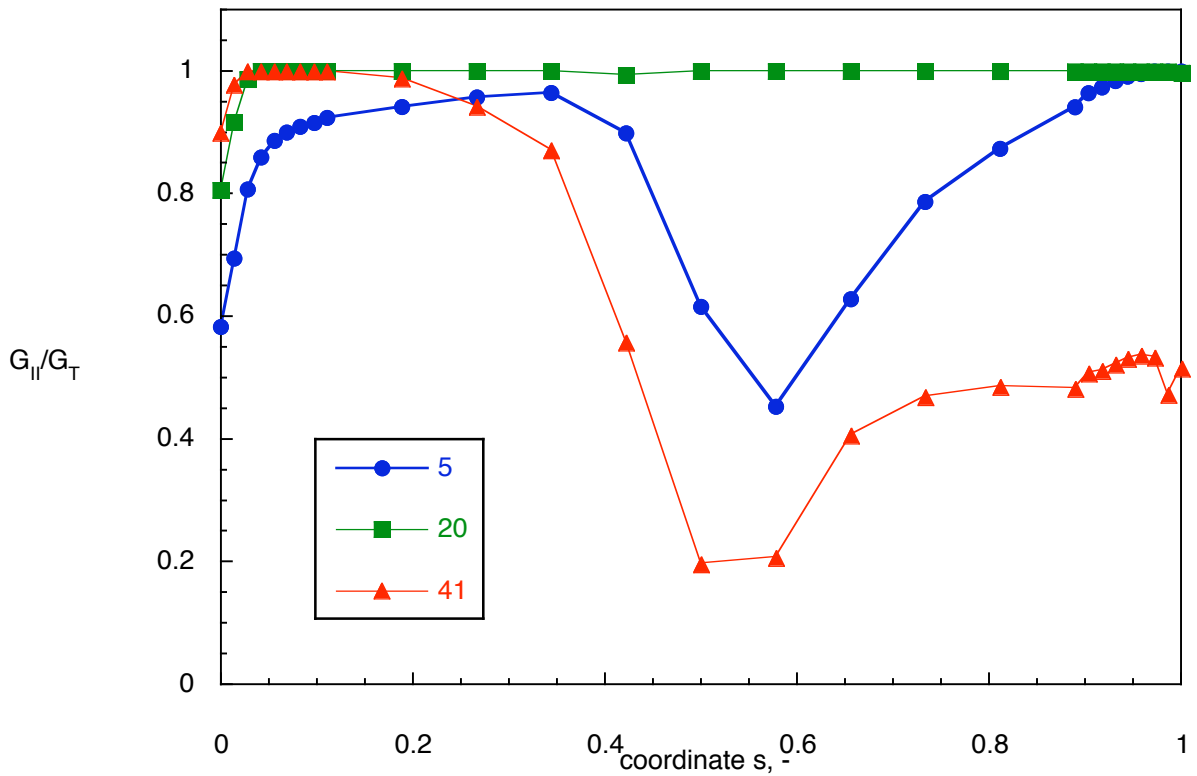


Figure 22. Computed mixed mode ratio across the width of the stringer for selected increments for delamination length $a=81.9$ mm.

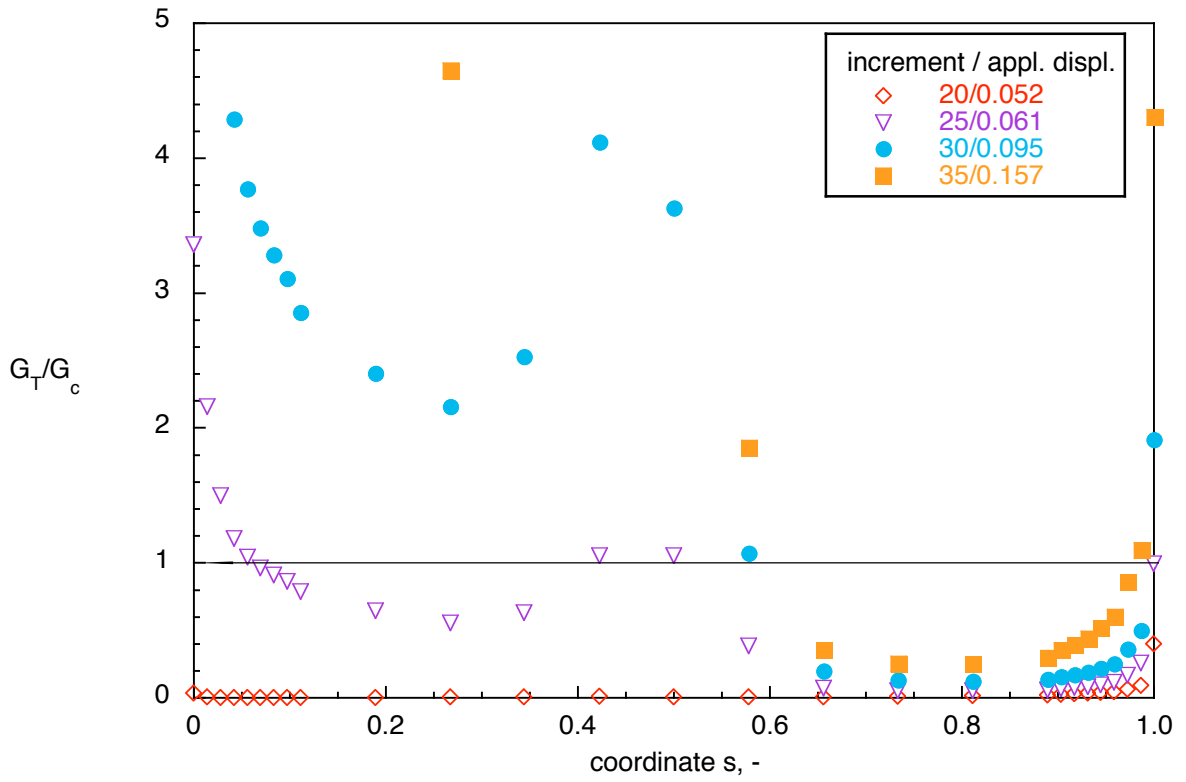


Figure 23. Computed failure index across the width of the stringer for selected increments for delamination length $a=81.9$ mm.

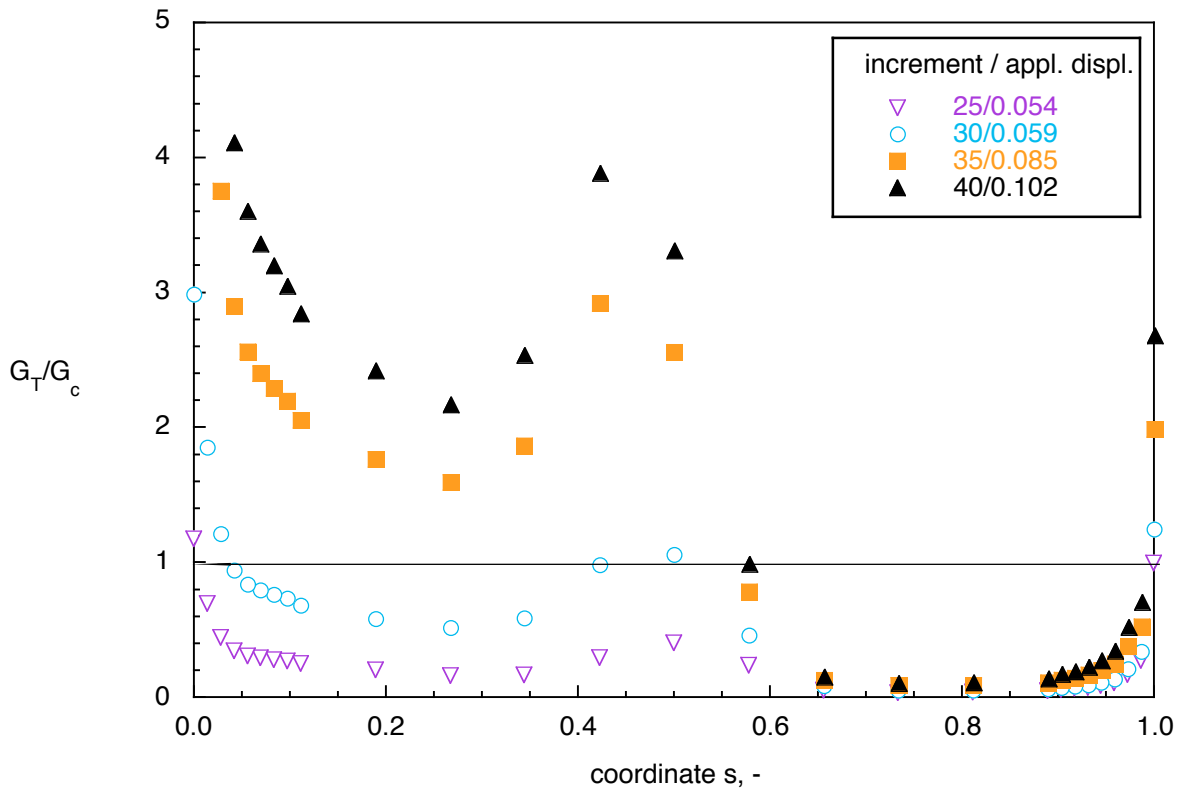


Figure 24. Computed failure index across the width of the stringer for selected increments for delamination length $a=88.9$ mm.

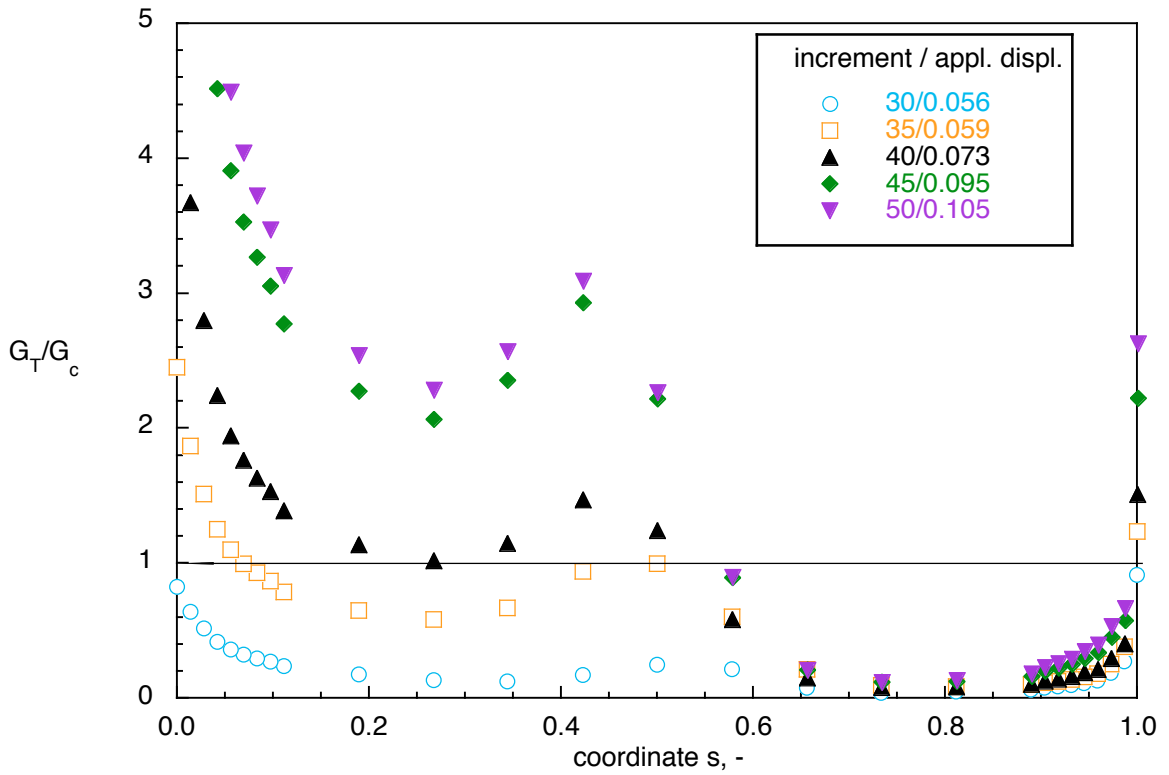


Figure 25. Computed failure index across the width of the stringer for selected increments for delamination length $a=94.6$ mm.

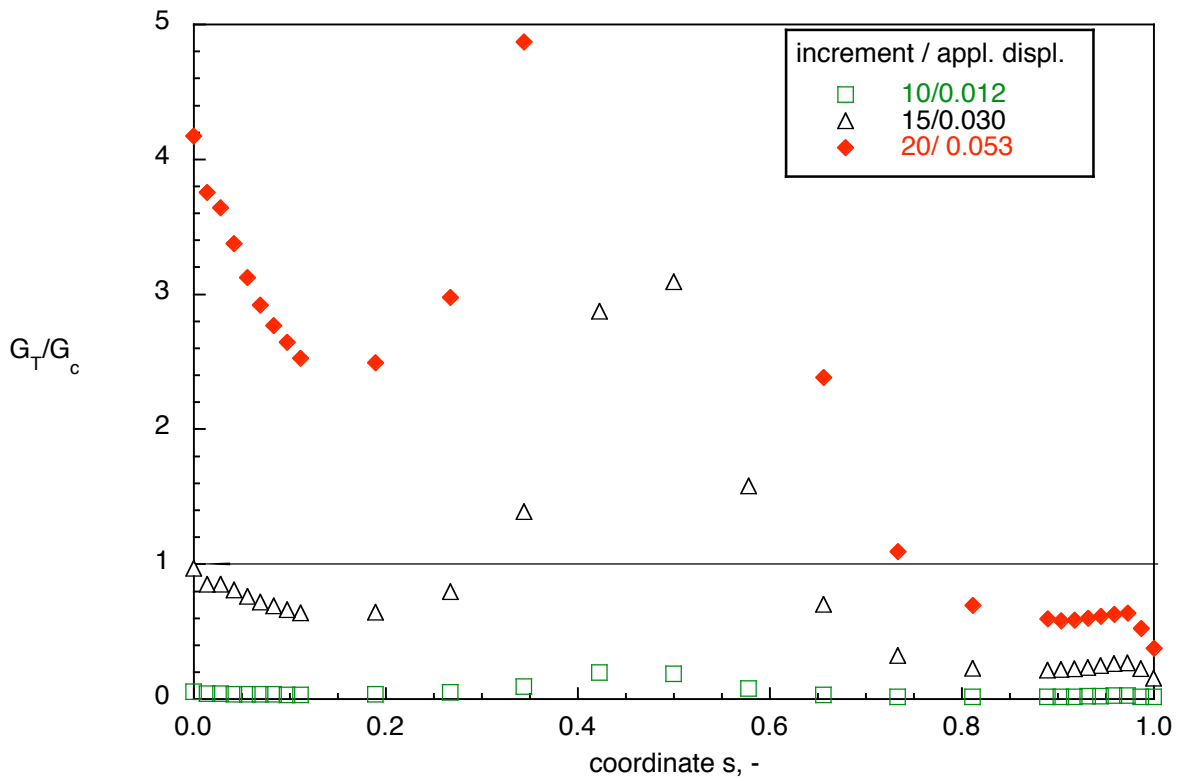


Figure 26. Computed failure index across the width of the stringer for selected increments for delamination length $a=101.6$ mm.

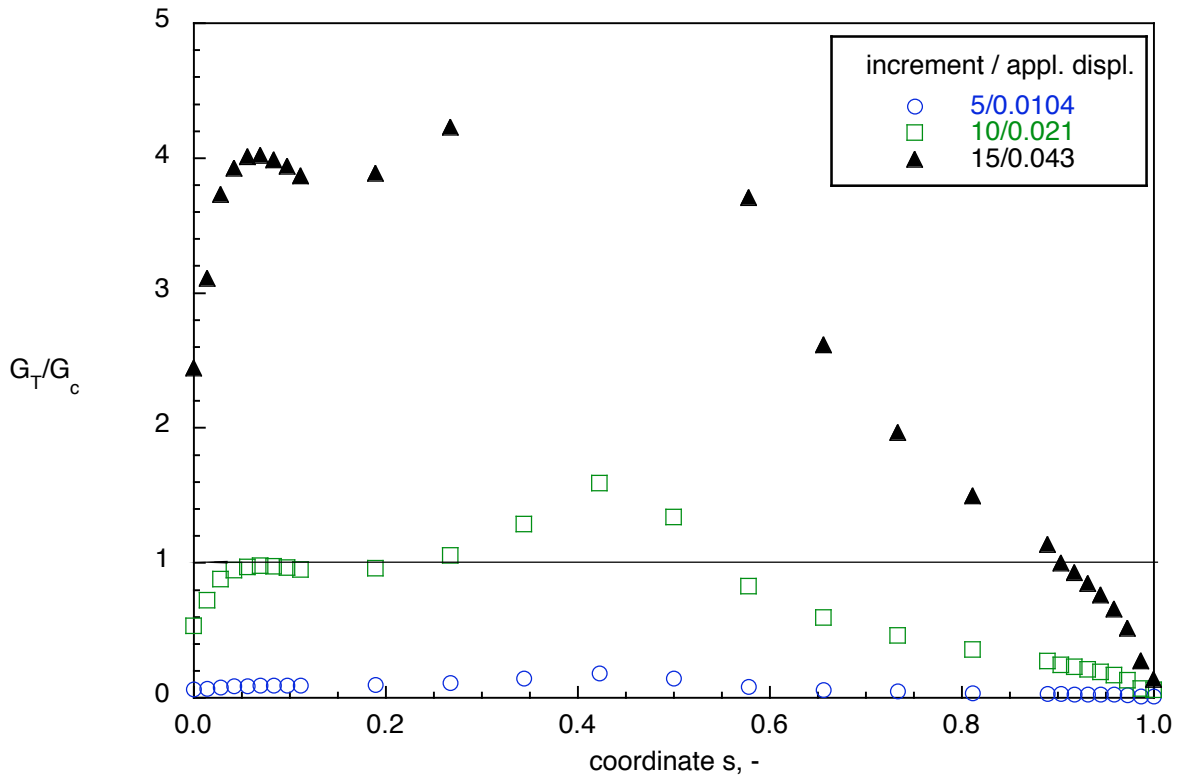


Figure 27. Computed failure index across the width of the stringer for selected increments for delamination length $a=127.0$ mm.

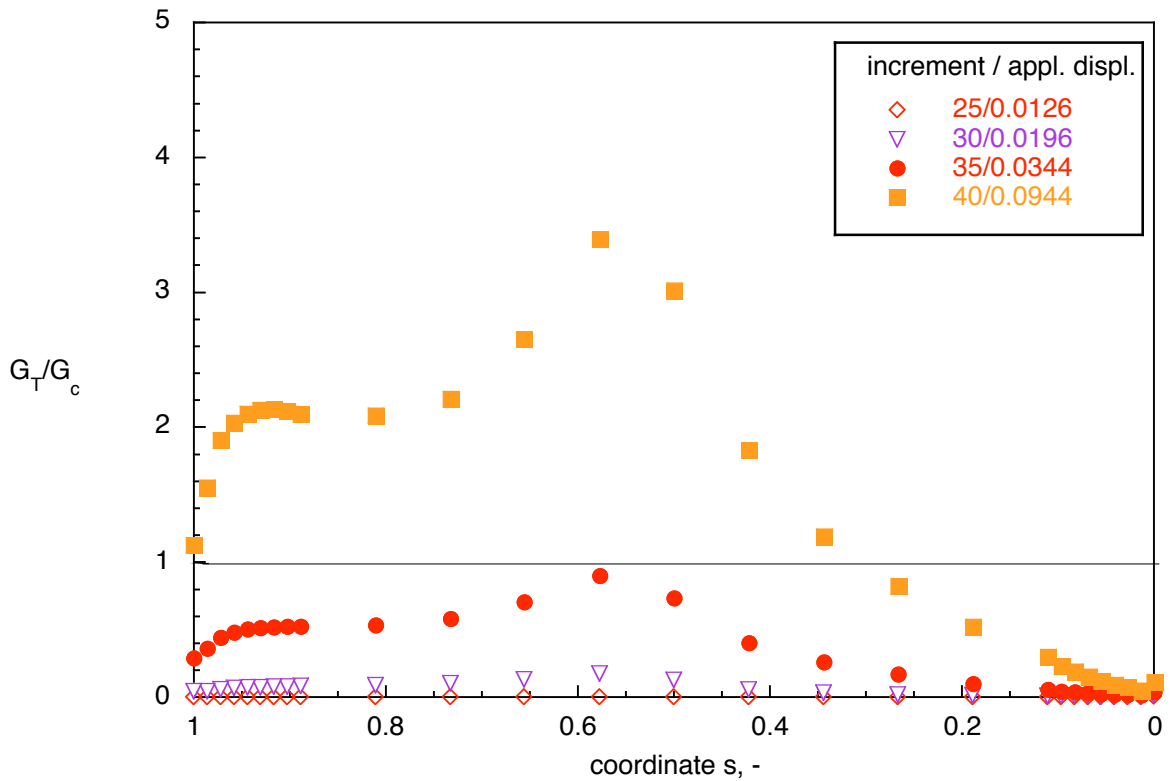


Figure 28. Computed failure index across the width of the stringer for selected increments for delamination length $a=203.2$ mm.

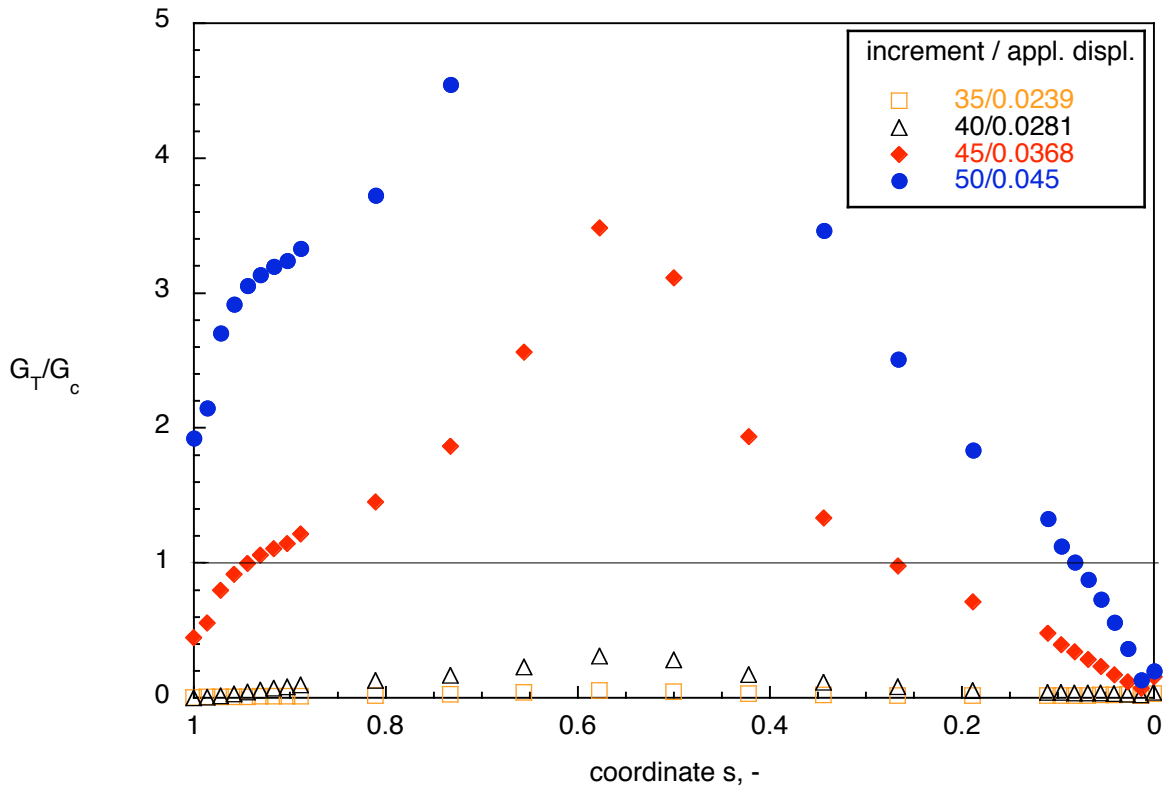


Figure 29. Computed failure index across the width of the stringer for selected increments for delamination length $a=279.4$ mm.

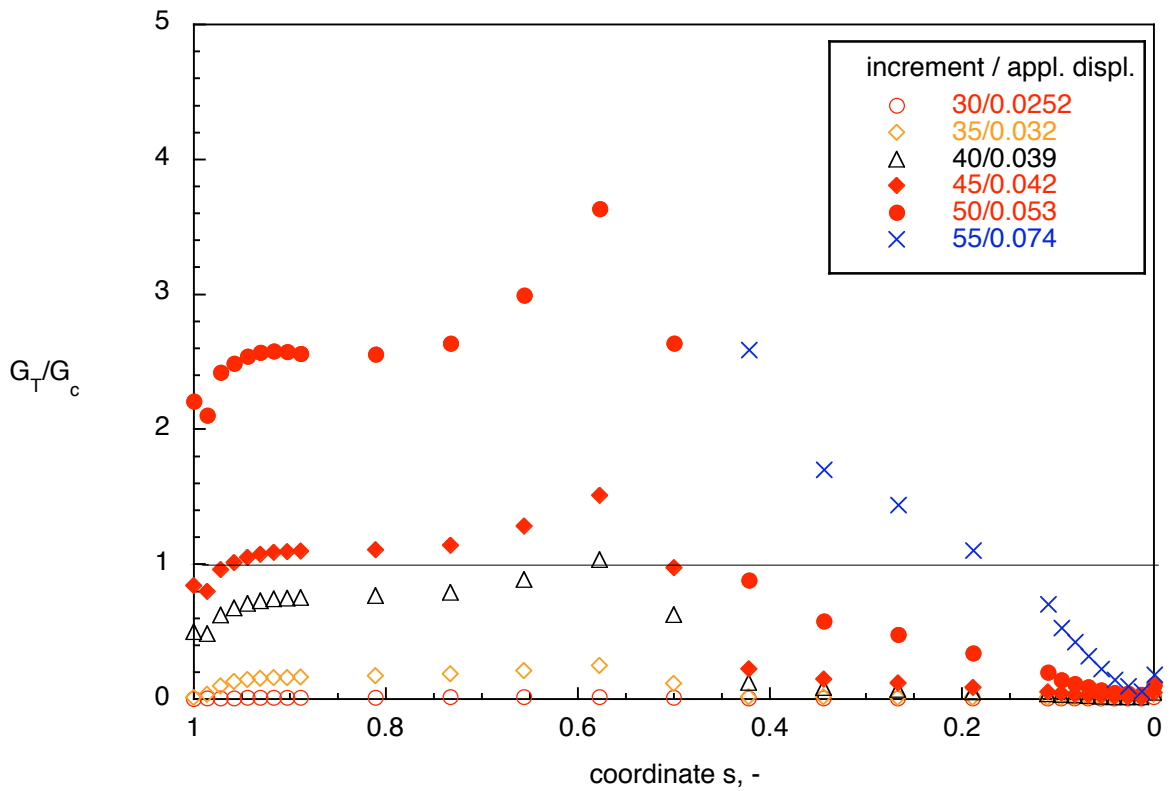


Figure 30. Computed failure index across the width of the stringer for selected increments for delamination length $a=355.6$ mm.

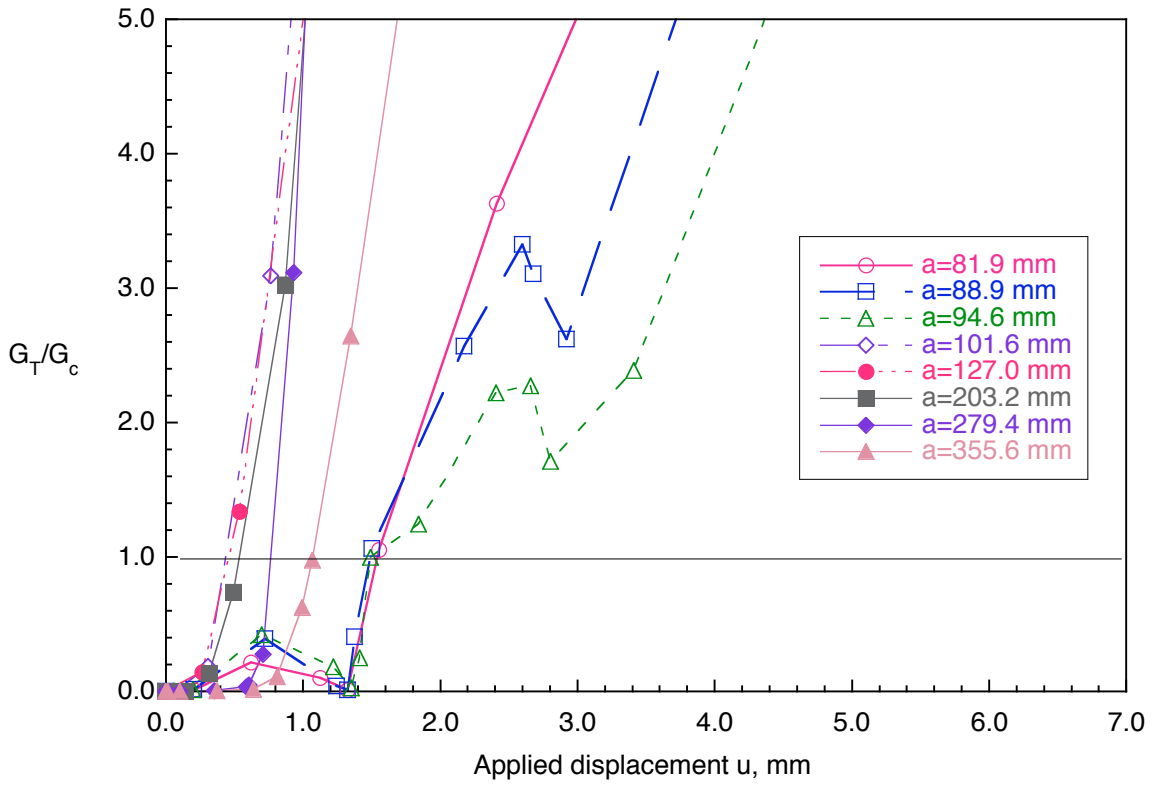


Figure 31. Failure index at the center of the stringer for different delamination lengths modeled.

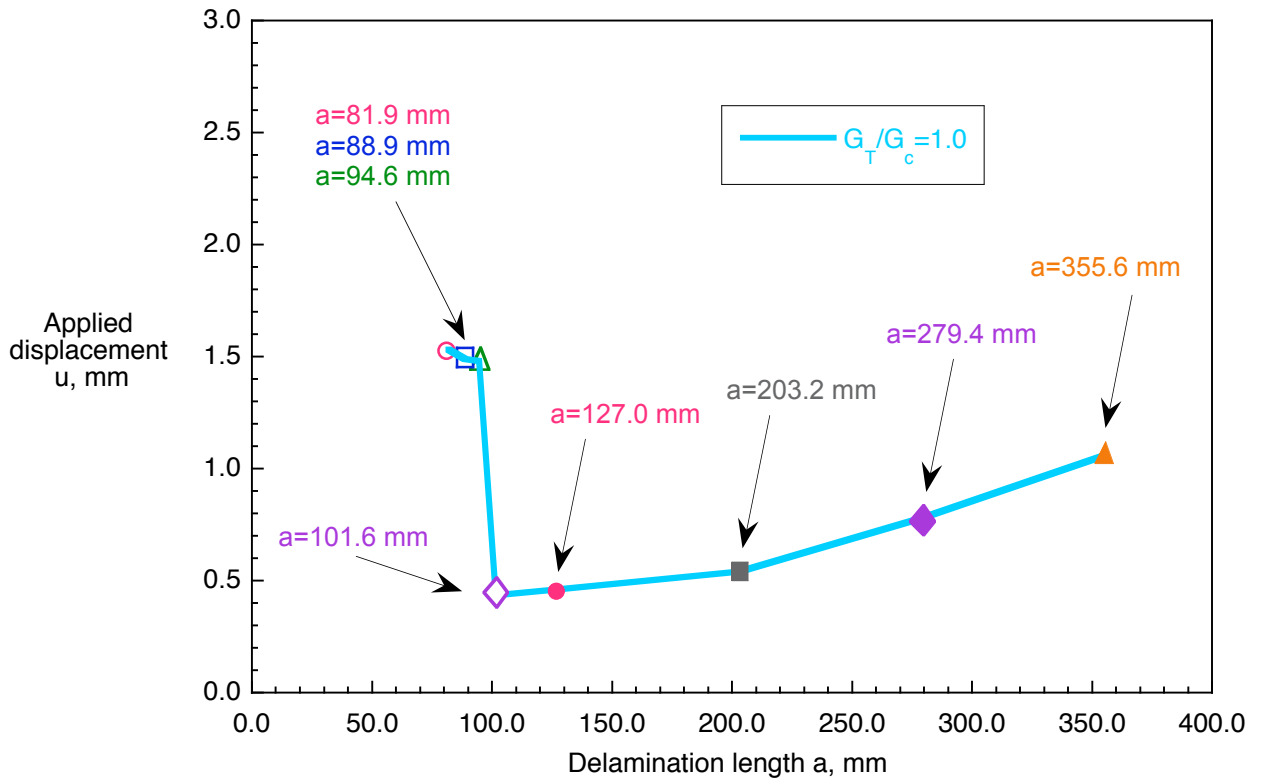


Figure 32. Applied external displacement at delamination onset for different delamination lengths modeled.

REPORT DOCUMENTATION PAGE

*Form Approved
OMB No. 0704-0188*

The public reporting burden for this collection of information is estimated to average 1 hour per response, including the time for reviewing instructions, searching existing data sources, gathering and maintaining the data needed, and completing and reviewing the collection of information. Send comments regarding this burden estimate or any other aspect of this collection of information, including suggestions for reducing this burden, to Department of Defense, Washington Headquarters Services, Directorate for Information Operations and Reports (0704-0188), 1215 Jefferson Davis Highway, Suite 1204, Arlington, VA 22202-4302. Respondents should be aware that notwithstanding any other provision of law, no person shall be subject to any penalty for failing to comply with a collection of information if it does not display a currently valid OMB control number.

PLEASE DO NOT RETURN YOUR FORM TO THE ABOVE ADDRESS.

1. REPORT DATE (<i>DD-MM-YYYY</i>)		2. REPORT TYPE		3. DATES COVERED (<i>From - To</i>)	
4. TITLE AND SUBTITLE			5a. CONTRACT NUMBER		
			5b. GRANT NUMBER		
			5c. PROGRAM ELEMENT NUMBER		
6. AUTHOR(S)			5d. PROJECT NUMBER		
			5e. TASK NUMBER		
			5f. WORK UNIT NUMBER		
7. PERFORMING ORGANIZATION NAME(S) AND ADDRESS(ES)				8. PERFORMING ORGANIZATION REPORT NUMBER	
9. SPONSORING/MONITORING AGENCY NAME(S) AND ADDRESS(ES)				10. SPONSORING/MONITOR'S ACRONYM(S)	
				11. SPONSORING/MONITORING REPORT NUMBER	
12. DISTRIBUTION/AVAILABILITY STATEMENT					
13. SUPPLEMENTARY NOTES					
14. ABSTRACT					
15. SUBJECT TERMS					
16. SECURITY CLASSIFICATION OF:			17. LIMITATION OF ABSTRACT	18. NUMBER OF PAGES	19a. NAME OF RESPONSIBLE PERSON
a. REPORT	b. ABSTRACT	c. THIS PAGE			19b. TELEPHONE NUMBER (<i>Include area code</i>)